

International Ocean Discovery Program Expedition 381 Preliminary Report

Corinth Active Rift Development

**Offshore expedition
19 October–18 December 2017**

**Onshore Science Party
31 January–28 February 2018**

Donna J. Shillington, Lisa C. McNeill, Gareth D.O. Carter, and the Expedition 381 Participants

Publisher's notes

Core samples and the wider set of data from the science program covered in this report are under moratorium and accessible only to Science Party members until 28 February 2019.

This publication was prepared by the European Consortium for Ocean Research Drilling (ECORD) Science Operator (ESO) and Texas A&M University (TAMU) as an account of work performed under the International Ocean Discovery Program (IODP). Funding for IODP is provided by the following international partners:

National Science Foundation (NSF), United States
Ministry of Education, Culture, Sports, Science and Technology (MEXT), Japan
European Consortium for Ocean Research Drilling (ECORD)
Ministry of Science and Technology (MOST), People's Republic of China
Korea Institute of Geoscience and Mineral Resources (KIGAM)
Australia-New Zealand IODP Consortium (ANZIC)
Ministry of Earth Sciences (MoES), India
Coordination for Improvement of Higher Education Personnel (CAPES), Brazil

Portions of this work may have been published in whole or in part in other IODP documents or publications.

Disclaimer

Any opinions, findings, and conclusions or recommendations expressed in this publication are those of the author(s) and do not necessarily reflect the views of the participating agencies or TAMU.

Copyright

Except where otherwise noted, this work is licensed under the Creative Commons Attribution 4.0 International (CC BY 4.0) license (<https://creativecommons.org/licenses/by/4.0/>). Unrestricted use, distribution, and reproduction are permitted, provided the original author and source are credited.



Citation

Shillington, D.J., McNeill, L.C., Carter, G.D.O., and the Expedition 381 Participants, 2019. *Expedition 381 Preliminary Report: Corinth Active Rift Development*. International Ocean Discovery Program.
<https://doi.org/10.14379/iodp.pr.381.2019>

ISSN

World Wide Web: 2372-9562

Expedition 381 participants

Expedition 381 scientists

Donna J. Shillington*

Co-Chief Scientist

Lamont-Doherty Earth Observatory
Columbia University
USA
djs@ldeo.columbia.edu

Lisa C. McNeill*

Co-Chief Scientist

Ocean and Earth Science
University of Southampton
National Oceanography Centre Southampton
United Kingdom
lcmn@noc.soton.ac.uk

Gareth D.O. Carter*

Expedition Project Manager

British Geological Survey
The Lyell Centre
United Kingdom
gcarter@bgs.ac.uk

Jeremy (Jez) Everest*

Expedition Project Manager

British Geological Survey
The Lyell Centre
United Kingdom
jdev@bgs.ac.uk

Erwan Le Ber*

Petrophysics Staff Scientist

School of Geography, Geology and the Environment
University of Leicester
United Kingdom
elb51@leicester.ac.uk

Richard Collier

Sedimentologist

Basin Structure Group
School of Earth and Environment
University of Leeds
United Kingdom
r.e.l.collier@leeds.ac.uk

Aleksandra Cvetkoska

Micropaleontologist (diatoms)

Department of Animal Ecology and Systematics
Justus Liebig University
Germany
acvetkoska@yahoo.com

Gino De Gelder

Structural Geologist

Institut de Physique du Globe de Paris
Sorbonne Paris Cité
Université Paris Diderot
France
gelder@ipgp.fr

Paula Diz Ferreiro*

Micropaleontologist (foraminifers)

Departamento Geociencias Marinas y Ordenación del
Territorio
Facultad de Ciencias del Mar
Universidad de Vigo
Spain
pauladiz@uvigo.es

Mai-Linh Doan

Petrophysicist (physical properties)

Université Grenoble Alpes
Université Savoie Mont Blanc
CNRS, IRD, IFSTTAR, and ISTerre
France
Mai-Linh.Doan@univ-grenoble-alpes.fr

Mary Ford

Structural Geologist/Sedimentologist

CRPG
UMR 7358
France

Also at

Université de Lorraine
ENSG
INP
France
Mary.ford@univ-lorraine.fr

Robert Gawthorpe*

Sedimentologist

Department of Earth Science
University of Bergen
Norway
rob.gawthorpe@uib.no

Maria Geraga

Micropaleontologist (foraminifers)

Department of Geology
University of Patras
Greece
mgeraga@upatras.gr

Jack Gillespie

Structural Geologist/Sedimentologist

Center for Tectonics, Resources, and Exploration (TRaX)
Department of Earth Sciences
School of Physical Sciences
University of Adelaide
Australia
Jack.gillespie@adelaide.edu.au

*Participated in shipboard and shore-based operations.

†Participated in shipboard operations only.

Romain Hemelsdaël**Sedimentologist**

Géosciences Montpellier
 Université de Montpellier
 France
r.hemelsdael@gmail.com

Emilio Herrero-Bervera**Paleomagnetist**

University of Hawaii at Manoa
 Hawaii Institute of Geophysics and Planetology
 USA
herrero@soest.hawaii.edu

Mohammad Ismaiel**Petrophysicist (physical properties)**

University Centre for Earth and Space Sciences
 University of Hyderabad
 India
ismaiel@iitdalumni.com

Liliane Janikian**Sedimentologist**

Departamento de Ciências do Mar
 Universidade Federal de São Paulo
 Brazil
lijanikian@gmail.com

Katerina Kouli**Micropaleontologist (palynology)**

Department of Geology and Geoenvironment
 National and Kapodistrian University of Athens
 Greece
akouli@geol.uoa.gr

Shunli Li**Sedimentologist**

School of Energy Resources
 China University of Geosciences (Beijing)
 China
lishunli@cugb.edu.cn

Malka Leah Machlus**Petrophysicist (physical properties)**

Lamont-Doherty Earth Observatory
 Columbia University
 USA

Also at

Department of Physical Sciences
 Kingsborough Community College
 City University of New York
 USA

machlus@ldeo.columbia.edu

Marco Maffione**Paleomagnetist**

School of Geography Earth and Environmental Sciences
 University of Birmingham
 United Kingdom
m.maffione@bham.ac.uk

Carol Mahoney**Inorganic Geochemist**

School of Earth and Environment
 The University of Leeds
 United Kingdom
c.mahoney@leeds.ac.uk

Georgios Michas**Petrophysicist (physical properties)**

Laboratory of Geophysics and Seismology
 Technological Educational Institute of Crete
 Greece
gmichas@hotmail.com

Clint Miller***Inorganic Geochemist**

Department of Earth, Environmental and Planetary Sciences
 Rice University
 USA
clint.m.miller@rice.edu

Casey Nixon**Structural Geologist**

Department of Earth Science
 University of Bergen
 Norway
casey.nixon@uib.no

Sabire Asli Oflaz**Micropaleontologist (foraminifers)**

Graduate School "Human Development in Landscapes"
 Christian-Albrechts-Universität zu Kiel
 Germany
aoflaz@gshdl.uni-kiel.de

Abah Philip Omale***Petrophysicist (physical properties)**

Department of Geology and Geophysics
 Louisiana State University
 USA
abahphilipomale@yahoo.com

Kostas Panagiotopoulos**Micropaleontologist (palynology)**

Institute of Geology and Mineralogy
 University of Cologne
 Germany
panagiotopoulos.k@uni-koeln.de

Sofia Pechlivanidou**Sedimentologist**

Department of Earth Science
 University of Bergen
 Norway
sofia.pechlivanidou@uib.no

Marcie Phillips***Micropaleontologist (nannofossils/diatoms)**

Institute for Geophysics
 University of Texas at Austin
 USA
marciepurkey@gmail.com

Simone Sauer***Inorganic Geochemist**

Ifremer
 Department of Marine Geosciences
 Centre Bretagne
 France
simone11sauer@gmail.com

Joana Seguin**Organic Geochemist**

Institute for Ecosystem Research
 Christian-Albrechts-Universität zu Kiel
 Germany
jseguin@ecology.uni-kiel.de

Spyros Sergiou***Sedimentologist**

Laboratory of Marine Geology and Physical Oceanography
 Department of Geology
 University of Patras
 Greece
sergiou@upatras.gr

Natalia Zakharova**Core-Log-Seismic Integration**

Department of Earth and Atmospheric Sciences
 Central Michigan University
 USA
n.zakh@cmich.edu

Operational and technical staff

ESO personnel and technical representatives

Ursula Röhl

Onshore Operations Manager/Laboratory and Curation Manager

Dave Smith[†]

Offshore Operations Manager

Malgorzata Bednarz

Petrophysics Technician

Vera B. Bender*

Data Manager

Liane Brück

Geophysics Technician

Laurent Brun[†]

Logging Engineer

Carol Cotterill

Outreach Manager

Douglas Cummings

IODP Publications Specialist (JRSO)

Nataliya Denchik

Petrophysics Technician

Volker Diekamp

Photographer

Alan Douglas*

IT Support

Thomas Friedrichs

Paleomagnetist

Patrizia Gepraegs*

Core Curator/Assistant Laboratory Manager

Sophie Green*

Expedition Project Manager

Nicole Kniebel

Micropaleontology/Palynology Technician

Brit Kokisch

Sedimentology Technician/LECO Operator

Martin Kölling

Inorganic Geochemistry Laboratory Manager

Holger Kuhlmann

Core Curator/IODP Bremen Core Repository Superintendent

Johanna Lofi

Petrophysicist

Vera Lukies

Petrophysics Technician

Garry McGowan[†]

Drilling Coordinator

Mary Mowat

Data Manager

Leah Nolan

Petrophysics Technician

Silvana Pape

Inorganic Geochemistry Laboratory Technician

Laurence Phillpot*

Petrophysics Technician

Ulrike Prange

Outreach Officer/Media Relations

Connor Richardson[†]

Drilling Coordinator

Pascal Robert[†]

Logging Engineer

Luzie Schnieders*

Geochemist

Apostolis Tsiligiannis[†]

Electrical Engineer

*Participated in shipboard and shore-based operations.

†Participated in shipboard operations only.

Graham Tulloch[†]
Drilling Coordinator

Christoph Vogt
XRD Laboratory Manager

Alex Wülbers*
Core Curator/Logistics

BCR/MARUM, University of Bremen (temporary student assistants)

Roles included core handling, core splitting, sampling, data entry, outreach, and catering

Eena Dadwal

Maret Ellinghausen

Johann Hollop

Sipan Issa

Lara Jacobi

Alex Manthey

Philip Meister

Ngozi Okoye

Nina Rohlf

Lara Steinbrink

Katharina Wetterauer

Rezan Yusef

D/V Fugro Synergy, Fugro N.V. (operational staff)

Artur Radomski[†]
Master

Sebastian Grzech[†]
Chief Officer

Stanislaw Gorniak[†]
1st Officer

Evert van den Berg[†]
2nd Officer

Vladislavs Leonovs[†]
2nd Officer

Krzysztof Jalowiecki[†]
Chief Engineer

Maksims Gerasimskis[†]
2nd Engineer

Tomasz Tchorzewski[†]
2nd Engineer

Gregorio Reyes[†]
3rd Engineer

Jonifer Orzal[†]
3rd Engineer

Christopher Boga[†]
3rd Engineer

Olivier Ouchene[†]
Survey

Golden Doe Bansah[†]
Survey

Grzegorz Przytarski[†]
Electrician

Roeland Baas[†]
Drilling Supervisor

Marcus Gerritse[†]
Electrician

Marcin Sos[†]
Rig Mechanic

Rafal Opelt[†]
Rig Mechanic

Gary Jago[†]
Party Chief

Tony Halliday[†]
Technical Lead

Rob Ammerlaan[†]
Senior Operator

Jeroen Kaandorp[†]
Senior Operator

Pieter van Leeuwen[†]
Operator

Tahsin Alkanat[†]
Operator

Eric Wessels[†]
Operator

Jeroen Stemmer[†]
Operator

James Bridge[†]
Drilling Supervisor

Max Harford[†]
Driller

Zander Kennie[†]
Driller

Matt Compton[†]
Driller

James Hood[†]
Driller

Geof Jelbert[†]
Driller

Sean Baxter[†]
Driller

Dan Williams[†]
Asst Driller

Chris Elliot[†]
Asst Driller

Adam Callaway[†]
Asst Driller

Matthew Rice[†]
Asst Driller

Thomas Mather[†]
Asst Driller

Liam Tregembo[†]
Asst Driller

Ronie Gutierrez[†]
A/B

Gilbert Amparo[†]
A/B

Marlon Bautista[†]
A/B

Rafael Monto[†]
A/B

Marvin Venturina[†]
A/B

Charlie Bardon[†]
Bosun

Pierre Sanidad[†]
Chief Cook

Neil Bandelaria[†]
Cook

Lim Leo[†]
Cook

Eric Elazegui[†]
Chief Steward

Rosenio Macabanti[†]
Steward

Zaldie Guerta[†]
Steward

Antonio Castro[†]
Steward

Zaldie Guerta[†]
Steward

Marvin Aguirre[†]
Steward

Romeo Romero[†]
Storekeeper

Elvin Octiza[†]
Storekeeper

Abstract

The primary objective of International Ocean Discovery Program Expedition 381 was to retrieve a record of early continental rifting and basin evolution from the Corinth rift, central Greece. Continental rifting is fundamental for the formation of ocean basins, and active rift zones are dynamic regions of high geohazard potential. However, the detailed spatial and temporal evolution of a complete rift system needed to understand rift development from the fault to plate scale is poorly resolved. In the active Corinth rift, deformation rates are high, the recent synrift succession is preserved and complete offshore, earlier rift phases are preserved onshore, and a dense seismic database provides high-resolution imaging of the fault network and of seismic stratigraphy around the basin. As the basin has subsided, its depositional environment has been affected by fluctuating global sea level and its absolute position relative to sea level, and the basin sediments record this changing environment through time. In Corinth, we can therefore achieve an unprecedented precision of timing and spatial complexity of rift-fault system development, rift-controlled drainage system evolution, and basin fill in the first few million years of rift history. The following are the expedition themes:

- High-resolution fault slip and rift evolution history,
- Surface processes in active rifts,
- High-resolution late Quaternary Eastern Mediterranean paleoclimate and paleoenvironment of a developing rift basin, and
- Geohazard assessment in an active rift.

These objectives were and will be accomplished as a result of successful drilling, coring, and logging at three sites in the Gulf of Corinth, which collectively yielded 1645 m of recovered core over a 1905 m cored interval. Cores recovered at these sites together provide (1) a longer rift history (Sites M0078 and M0080), (2) a high-resolution record of the most recent phase of rifting (Site M0079), and (3) the spatial variation of rift evolution (comparison of sites in the central and eastern rift). The sediments contain a rich and complex record of changing sedimentation, sediment and pore water geochemistry, and environmental conditions from micro-paleontological assemblages. The preliminary chronology developed by shipboard analyses will be refined and improved during postexpedition research, providing a high-resolution chronostratigraphy down to the orbital timescale for a range of tectonic, sedimentological, and paleoenvironmental studies. This chronology will provide absolute timing of key rift events, rates of fault movement, rift extension and subsidence, and the spatial variations of these parameters. The core data will also allow us to investigate the relative roles of and feedbacks between tectonics, climate, and eustasy in sediment flux and basin evolution. Finally, the Corinth rift boreholes will provide the first long Quaternary record of Mediterranean-type climate in the region. The potential range of scientific applications for this unique data set is very large, encompassing tectonics, sedimentary processes, paleoenvironment, paleoclimate, paleoecology, geochemistry, and geohazards.

Introduction

How rifting initiates and evolves to continental breakup and ocean basin formation is a major unanswered solid earth/plate tectonic question; continental rifting is the first stage of this process.

Numerical models indicate that strain rate is a key parameter controlling the style and magnitude of extension, but spatial and temporal patterns in strain rate are very poorly known for most extensional systems due to scarce chronological constraints, other than over short (earthquake-cycle) timescales. Key questions include the following: What controls rift geometry and evolution? How does activity on faults change with time? What does rift evolution and fault activity tell us about crustal rheology? What are the implications of changing fault activity for earthquake activity in a developing rift fault system? Over the last ~15 years, important insights have been derived from numerical models (e.g., Burov and Poliakov, 2001; Lavier and Buck, 2002; Lavier and Manatschal, 2006; Huismans and Beaumont, 2007, 2011; Olive et al., 2014) and from observations at mature, magma-poor passive margins where activity has ceased (e.g., Manatschal et al., 2001; Whitmarsh et al., 2001; Osmundsen and Ebbing, 2008; Van Avendonk et al., 2009; Bayrakci et al., 2016). However, early synrift stratigraphy is often difficult to image and sample due to deep burial and tectonic overprinting, making it difficult to examine the earliest stages of rifting.

Instead, this project studies the young, seismically active Corinth rift with a unique existing data set to resolve at high temporal and spatial resolution how rift faults initiate and link and how strain is distributed over time. The rift is currently a closed, small-scale clastic sedimentary system, and the last ~1–2 My of the synrift stratigraphic record is preserved offshore, with earlier rift sediments preserved onshore, providing a clear spatial and temporal record of fault and rift activity. The Corinth rift is also an ideal target for studying rift processes because it is opening orthogonally (perpendicular to the rift axis) at high strain rates (e.g., Briole et al., 2000), extension is focused with well-constrained initial conditions, it lacks volcanism, and there is almost no tectonic overprinting. Thus, the number of variables contributing to rift development are reduced, and a study here will complement research in other active rift systems that are more mature, oblique, and/or characterized by significant magmatism (e.g., East Africa and the Gulf of California).

Constraining the contributions of tectonics and climate to landscape evolution and sediment delivery in active basins and how surficial processes influence rifting remains another major challenge in Earth science. Uplift and subsidence associated with rift faults can strongly modify landscapes, creating and destroying sediment delivery pathways into rift basins (e.g., Gawthorpe and Leeder, 2000), but a detailed record of a complete sedimentary system in a young, active rift is lacking. For example, how do strain rate and strain distribution control landscape development and sediment flux into rifts? Climate is clearly another dominant control on sediment flux. Isolated and semi-isolated basins formed by rifting are particularly sensitive to climate and global climate-driven sea level change (e.g., Collier et al., 2000; Scholz et al., 2007; McHugh et al., 2008); thus, active rift basins are ideal targets both for assessing how changing climate impacts sedimentation and for examining changes in paleoenvironment as basins become isolated and then reconnected to the global oceans. Where strain rates are high, such as at the Corinth rift, high basin sediment accumulation rates provide a very high resolution record of regional climate, basin paleoenvironment, and change in sediment source and flux into the basin through time. Recent models predict that surface processes will also strongly influence rift development by modifying the thermal structure (Bialas and Buck, 2009) and by redistributing mass through erosion and deposition (Olive et al., 2014), all of which can influence

fault evolution and strain localization. Addressing all of these questions, determining driving mechanisms, and resolving the interplay between processes requires a detailed record of climate, tectonics, and sedimentation in a young rift basin. The Corinth rift is an excellent location to tackle these questions. Glacial–interglacial cycles are characterized by changes in climate, sea level, and vegetation, including in this region (e.g., Tzedakis et al., 2009; Sadori et al., 2016), allowing us to examine the impact of both climatic change and tectonics on surface processes. Sedimentation rates are high, and the geology around the Corinth rift is well studied, enabling a comprehensive study of the complete synrift sedimentary system.

During International Ocean Discovery Program (IODP) Expedition 381 we drilled, sampled, and logged a significant part of the synrift sequence of the Corinth rift to constrain in space and time the deformation rate, absolute timing of rifting processes, subsidence and sediment flux, changing paleoenvironment and depositional conditions, and the interaction of rift development and climate on surface processes and sediment flux.

Background

The Corinth rift

The Corinth rift (Figure F1) is one of Europe's most seismically active areas. The Aegean Sea represents a natural laboratory for the study of rapid continental extensional tectonics, with extension beginning in the Oligocene–Miocene (e.g., McKenzie, 1978; Le Pichon and Angelier, 1981; Jolivet et al., 1994; Armijo et al., 1996; Jolivet, 2001). In the late Pliocene–early Pleistocene, deformation became strongly localized across a few zones, and the Corinth rift was the most prominent. The active rift is a ~100 km × 30–40 km band experiencing north–south extension, and the entire rift system is ~70–80 km wide. Current extension rates reach 10–15 mm/y (e.g., Clarke et al., 1998; Briole et al., 2000; Bernard et al., 2006), some of the highest in the world, giving strain rates of $\sim 5 \times 10^{-7}/y$. Debate continues on the origin of extension in the broader Aegean and focusing of strain at the Corinth rift, with models typically combining gravitational collapse of thickened crust, subduction-driven roll-back and back-arc extension, westward expulsion of Anatolia, and propagation of the North Anatolian fault (e.g., Armijo et al., 1996; Jolivet et al., 2010). Regional lithospheric structure, including crustal thickness and structure of the underlying subducting African plate, is constrained by wide-angle seismic and teleseismic tomographic techniques and gravity data (e.g., Tiberi et al., 2000; Sachpazi et al., 2007; Zelt et al., 2005); thicker crust (~40–45 km) runs northwest–southeast along the orogenic Hellenide/Pindos mountain belt in the western rift.

Rift evolution and stratigraphy

Corinth rifting began at ~5 Ma with three main phases identified by integration of onshore depositional records and offshore seismic stratigraphy (Figure F2) (e.g., Higgs, 1988; Armijo et al., 1996; Sachpazi et al., 2003; Ford et al., 2007; Bell et al., 2009; Taylor et al., 2011; Nixon et al., 2016; Gawthorpe et al., 2017). Initial Pliocene basal deposition (from onshore preserved sediments) was continental, varying from alluvial fans in the west to lakes in the east (“Lower Group”) (Ford et al., 2007, 2013; Rohais et al., 2007; Hemelsdaël et al., 2017). Increased subsidence rates, depocenter deepening, and fault linkage followed, with large marginal fan deltas (locally >800 m thick) now uplifted and exposed onshore (“Middle Group”; Backert et al., 2010). The timing of the depocenter deepening

and transition from the Lower Group to Middle Group may have occurred at different times along the rift (e.g., ~2.2 Ma in the Alkyonides Gulf [eastern rift], ~3.0 Ma in the central rift [Leeder et al., 2008, 2012], and ~1.8 Ma in the western rift [Ford et al., 2013]). This transition is thought to represent increased subsidence and sediment supply into the rift at the location of the modern Gulf of Corinth (Middle Group onshore; proposed correlation with the lower synrift unit [seismic Unit 1] offshore). During this phase, the rift was controlled by both south- and north-dipping bounding faults (Bell et al., 2009; Ford et al., 2013, 2016; Nixon et al., 2016).

At ~0.6 Ma (hypothesized age prior to drilling), fault activity stepped northward and the rift narrowed, establishing the modern rift asymmetry with southern boundary north-dipping faults dominating subsidence and with new fan deltas developing along the southern gulf margin (“Upper Group” onshore; upper synrift unit [seismic Unit 2] offshore). These southern boundary faults apparently grew and linked rapidly (Nixon et al., 2016). During this time, the rift environment was hypothesized to alternate between isolated/semi-isolated and marine between glacial and interglacial periods, respectively, as eustatic sea level fluctuated relative to the boundaries of the basin (west: Rion sill; east: Isthmus of Corinth). The exact onset of regular marine deposition is not known but is hypothesized to correlate with the distinct seismic stratigraphy of the offshore upper synrift unit, seismic Unit 2 (Bell et al., 2009; Nixon et al., 2016). However, earlier limited marine incursions have been described (e.g., Bentham et al., 1991; Ford et al., 2007, 2013).

The rift appears to have narrowed as it evolved (strain localization) but also migrated northward. Geodetic and microseismicity data indicate the highest modern strain rates in the western rift (e.g., Avallone et al., 2004; Bernard et al., 2006). However, long-term extensional strain (geological timescales) is greatest in the central rift (e.g., Bell et al., 2009, 2011). The extension rate may have increased at specific times over rift history (Ford et al., 2013, 2016), suggesting a deviation from models with relatively constant net strain and increasing, gradual localization (McLeod et al., 2000; Sharp et al., 2000; Gawthorpe et al., 2003; Taylor et al., 2004).

Offshore rift architecture and synrift stratigraphy

Patterns of extension in the offshore rift change along axis and with time, with changing polarity and symmetry of fault networks, single versus multiple active faults, and complex and changing depocenter geometry offshore (Figures F1, F3). Clear, traceable unit boundaries (possible unconformities or sequence boundaries) mark major changes in rift development, but their age is unknown.

The synrift succession offshore is locally as thick as ~2.5 km and divided into two seismic stratigraphic units separated by a locally angular unit boundary or unconformity (U): the older, lower amplitude seismic Unit 1 and the younger, well-stratified, and higher amplitude seismic Unit 2 (e.g., Figures F4, F5, F6, F7). Seismic Unit 1 includes two different seismic facies that may or may not be stratigraphically distinct: a nonstratified (limited clear reflections) subunit (1a) mainly found on the southern basin margin and a more widespread, stratified (although weakly in places) subunit (1b) (see Nixon et al., 2016). Seismic Unit 2 has been interpreted to record glacial–interglacial cycles on the basis of marine and lacustrine conditions detected in short cores (Sachpazi et al., 2003; Moretti et al., 2004), clinoform sequences on some basin margins (e.g., Leeder et al., 2005; McNeill et al., 2005; Lykousis et al., 2007; Bell et al., 2008), and alternating low-amplitude/high-amplitude seismic sequences interpreted as lowstand lacustrine/highstand marine sequences, re-

spectively (e.g., Sachpazi et al., 2003; Lykousis et al., 2007; Bell et al., 2008, 2009; Taylor et al., 2011) (e.g., Figure F5). The integrated sequence stratigraphic interpretations suggest the base of seismic Unit 1 is ~0.6 Ma (Nixon et al., 2016). The onshore Middle Group is thought to be time-equivalent to seismic Unit 1 offshore, with the onshore Upper Group equivalent to seismic Unit 2 offshore. The onshore Lower Group is likely of minimal thickness offshore, if present at all, being north of the primary locus of rifting at that time. However, earlier rift phases (such as those in the Megara basin in the eastern rift; e.g., Bentham et al., 1991) may have extended into the present-day offshore rift area in the Alkyonides Gulf, at the eastern end of the rift (Figure F1).

Depth to basement maps (Bell et al., 2009; Taylor et al., 2011) show a single depocenter below the current central gulf, with reduced subsidence in the eastern (Alkyonides Gulf) and western rift. Isochore maps of the synrift sediments (Figure F3; Bell et al., 2009; Taylor et al., 2011; Nixon et al., 2016) indicate that before the ~0.6 Ma unit boundary/unconformity separating seismic Units 1 and 2, two primarily symmetric depocenters existed, but since ~0.6 Ma, these have linked into a single depocenter, coincident with transfer of strain from south- to north-dipping faults (increased asymmetry). Specifically, a change in rift polarity and symmetry followed by depocenter linkage occurred. The switch to dominant north-dipping faults appears to be broadly synchronous along the entire rift. Since ~200 ka, these north-dipping faults appear to have evolved by linkage of smaller fault segments into longer fault segments and have increased in displacement and activity with equivalent changes to the associated depocenters. The timing and rate of switch in rift polarity/symmetry and of fault and depocenter linkage could only be constrained by drilling that can provide chronostratigraphy combined with the existing dense seismic network.

Changing paleoenvironment in the Corinth area

Minimal information is available on the impact of climate variations and resulting sea level changes on sedimentation and paleoenvironment in the Corinth rift. Existing constraints come from onshore studies (e.g., Andrews et al., 2007), piston cores as long as 30 m (e.g., Moretti et al., 2004) and geophysical imaging (e.g., Perissoratis et al., 2000; Bell et al., 2009). Late Quaternary interglacials in southeastern Europe are characterized by Mediterranean, sub-Mediterranean, and temperate forests, whereas glacial cycles are characterized by open woodland and steppes (e.g., Tzedakis et al., 2009; Sadori et al., 2016). Systematic fluctuations in marine microfossil assemblages and in the isotopic composition of their shells depict long- and short-term climatic changes in the region. In addition, these fluctuations provide valuable information regarding the impact of both African monsoon variability and higher latitude climate processes on the climatic and oceanographic evolution of the Eastern Mediterranean Sea (e.g., Rohling et al., 2015). Glacial–interglacial cycles appear to be associated with changes in sedimentary processes and environment in the Corinth basin (e.g., Perissoratis et al., 2000); for example, long piston cores that sample the most recent transition reveal changes in sediment facies and micropaleontological assemblages (Moretti et al., 2004). The collection of cores and data from drilling will provide unique constraints for examining the impact of both climatic change and tectonics on sedimentation and paleoenvironment in the gulf and improving understanding of regional climate in the Quaternary.

Objectives

Primary objectives

1. *Fault and rift structural evolution in an active continental rift: to establish the distribution of tectonic strain in time and space and the timescales of fault evolution in a young rift at high resolution (20–50 ky and one to tens of kilometers).*

We will determine the growth and development of a rift-scale normal fault network, timescales of segmentation establishment, basin evolution in terms of strain localization, rift propagation and migration, and the impact of crustal structure and composition on strain rate and distribution. What are the controlling parameters on strain localization? How and when does a “mature” fault network emerge? How does fault evolution impact subsidence patterns and depocenter development?

2. *Surface processes in active rifts: to determine the evolution of a rift-controlled, closed drainage system in time and space at high temporal resolution (20–50 ky) and the relative impact of tectonics and climate on sediment flux.*

What are the relative contributions of millennial to orbital periodicity Quaternary climate fluctuations (global and regional) and fault activity/rift evolution in controlling the supply of sediment into a rift basin? We will assess changes in sediment flux at a range of timescales and analyze the paleoenvironment of the rift basin through time. These results will be used to evaluate the response of sediment supply to fault birth, death and migration, rift flank uplift, and changes in strain rate and to better understand feedbacks between climate, sea level fluctuations, erosion, sediment transport, and deposition and tectonic processes.

Secondary objectives

3. *To resolve reliable active fault slip rates to improve regional assessment of hazards due to earthquakes and secondary tsunamis and landslides.*

The Gulf of Corinth has high levels of seismicity and damaging historic secondary hazards such as slope failure and tsunami in a region of high coastal population density and tourism. Fault slip rates currently rely on paleoseismological and tectonic geomorphological studies with dated materials of very recent fault slip (the last ~200 ky or less) and estimated horizon ages for longer timescales. These slip rate estimates include significant uncertainties, and slip rates remain unquantified on many faults. Ocean drilling allows us to determine fault slip rates on timescales of 10–100 ky to 1 My. We will integrate fault slip rates with shorter timescale data (paleoseismological, geodetic, and seismicity) to more fully understand the seismic hazard potential of individual faults. Cores may also allow us to assess the frequency of major slope failures (integrated with seismically identified mass transport deposits offshore), an indication of secondary hazards and of possible seismicity.

4. *To generate a new high-resolution record of the Quaternary paleoclimate of the Eastern Mediterranean Sea with respect to global climate and the paleoenvironment of the Corinth basin as a semi-isolated marine-lacustrine basin controlled by changing base level and climate.*

Details of the Corinth basin's changing environment from glacial to interglacial times are poorly known, and the precise timing and nature of transitions between isolated and marine conditions is

unconfirmed, as is the relationship to the interacting controls of basin subsidence, sill elevation, and eustatic sea level. Offshore drilling of synrift sediments provides a record of regional Quaternary paleoclimate and basin paleoenvironment by sampling and analyzing pollen, micro- and macrofossils, stable isotopes, and sediment physical and chemical properties. Long cores from the Gulf of Corinth will also provide the opportunity to generate (1) the first high-resolution relative paleointensity (RPI) record in the Mediterranean Sea correlated with global RPI stacks (e.g., Valet et al., 2005; Channell et al., 2009) and the pattern of the magnetic excursions (Stott et al., 2002; Lund et al., 2005; Channell et al., 2008) to help understand the dynamics of the geomagnetic field and (2) a linked terrestrial pollen and marine $\delta^{18}\text{O}$ record in the Eastern Mediterranean Sea (at least for interglacial intervals) to establish a record of paleoenvironment and vegetation and to help constrain age models for existing Eastern Mediterranean long pollen records.

Operational strategy

Based on seismic and bathymetric data acquired in the Gulf of Corinth prior to the expedition, three primary and three alternate drill sites were proposed to satisfy the objectives of the proposal. The three primary (and ultimately drilled) sites (Figure F1) were selected based on the likelihood of recovering key stratigraphic units to achieve the expedition scientific objectives, the ability to correlate with horizons in the seismic reflection data network, and, in combination, to resolve both temporal and spatial rift evolutionary history.

Site M0078 (proposed Site COR-02A) is located in the central basin on a horst block where there is therefore a relatively condensed section. This site allows recovery of a long synrift record, including a significant part of seismic Unit 1 below, a near-complete seismic Unit 2 above, and the regional unit boundary or unconformity between them (Figures F4, F5). Site M0079 (proposed Site COR-01A) allows sampling of a complete seismic Unit 2 at very high resolution (Figures F4, F6). Site M0080 (proposed Site COR-04B) was selected because the uppermost basement and early seismic Unit 1 sediments can be sampled at this location due to the relatively thin seismic Unit 2 section (Figures F4, F7). The location of Site M0080 in the eastern part of the rift (Alkyonides Gulf; Figure F1) also provides an opportunity to test along-axis variation in rift processes.

All holes were sited in a 20 m radius of the proposed drilling sites approved by the IODP Environmental Protection and Safety Panel (EPSP), with Holes M0078A, M0079A, and M0080A all situated within 5 m of the specified coordinates. The general locations of the sites drilled are shown in Figure F1. As with all Mission Specific Platform expeditions, no cores were split during the offshore phase; therefore, a comprehensive onshore phase complemented the offshore phase. Table T1 summarizes the descriptions and measurements made during Expedition 381 and indicates whether they were conducted offshore or onshore.

Offshore operations

Mobilization of the vessel began on 3 October 2017 in Falmouth, UK, with the D/V *Fugro Synergy* sailing for the Port of Valletta, Malta, on 7 October. On 16 October, the vessel arrived at the

Port of Valletta, and European Consortium for Ocean Research Drilling (ECORD) Science Operator (ESO) personnel joined the vessel to continue the mobilization of science facilities before arrival in Greece. Following refueling, the *Fugro Synergy* continued the transit to the Port of Corinth, Greece, and was alongside on 19 October.

The offshore phase took place from 19 October to 18 December. The vessel sailed from Corinth on 22 October and returned to port on 18 December. Demobilization also took place at the Port of Corinth, where the ESO refrigerated (reefer) containers, containerized laboratories, multisensor core logger (MSCL) laboratory container, and offices were offloaded from the vessel in preparation for road transport to the Center for Marine Environmental Sciences (MARUM), University of Bremen (Germany), and transfer to Pireás, Greece, for shipping by sea to the British Geological Survey (UK). The University of Montpellier logging container was transported by sea to Falmouth (UK) and then over land to Montpellier. ESO staff departed by 19 December following completion of demobilization.

The cores, core catcher samples, headspace gas samples, and interstitial water splits collected offshore were transported under refrigeration to the IODP Bremen Core Repository at MARUM (University of Bremen, Germany).

In total, 52.5 days of Expedition 381 were spent operational on station, 0.5 days were spent in transit between sites, 0.8 days were spent in port during the expedition, 0.2 days were spent on standby at station because of weather, and 2.3 days were spent on equipment-related downtime. See Table T2 for a summary of offshore operations and recovery. Shipboard-generated recovery plots are available in the weekly ship reports on the ECORD Expedition 381 website (<http://www.ecord.org/expedition381/reports>).

The following coring and downhole logging tools were available during Expedition 381:

- Fugro Wilson Extended Piston (WEP) system (designated “H”),
- Fugro Corer system in push mode (designated “P”) and percussive mode (designated “V”),
- Fugro Extended Marine Core Barrel (FXMCB) system (rotary; designated “R”),
- DOSECC Exploration Services suite of coring tools as a backup, and
- A suite of standalone and stackable slimline wireline logging tools (from the University of Montpellier and operated by the European Petrophysics Consortium).

Onshore Science Party

Thermal conductivity measurements were carried out on all cores before the start of the Onshore Science Party (OSP).

During the Expedition 381 OSP from 31 January to 28 February 2018, the cores were described in detail and IODP standard sampling and measurements and postexpedition scientific research sampling were undertaken (Table T1). Analytical laboratories and equipment were used at MARUM (nondestructive core logging, marine geotechnics, inorganic geochemistry, and microscopes) and the Department of Geosciences at the University of Bremen (paleomagnetism and hydrofluoric acid laboratories and the carbon/sulfur analysis system).

Principal results

Operational site summaries

Site M0078

Site M0078 is located in the central Gulf of Corinth (Figure F1) on a fault-bounded horst block (Figure F5) with the aim of recovering a long, condensed record of synrift sedimentation. Two holes (M0078A and M0078B) were drilled at water depths of ~860 meters below sea level (mbsl). Hole M0078A was drilled and cored to 610.43 meters below seafloor (mbsf) using the Fugro WEP system (piston), the Fugro Corer in push and percussive modes, and the FXMCB (rotary corer). Core recovery was 87%. Downhole logging was attempted in Hole M0078A but successful data collection was not possible. Hole M0078B was drilled and cored to 55.85 mbsf using the Fugro Corer in push mode to capture material not recovered in Hole M0078A. Core recovery was 93%. Downhole logging was not conducted in Hole M0078B because it was a relatively shallow hole.

Site M0079

Site M0079 is located in the central Gulf of Corinth (Figure F1) with the aim of drilling a complete and expanded stratigraphic section of the most recent rift phase and the uppermost section of sediments from the penultimate phase to provide a high-resolution temporal record (Figure F6). Hole M0079A (water depth of 857 mbsl) was drilled and cored to 704.9 mbsf using the Fugro Corer in push and percussive modes and the FXMCB. Core recovery was 87%. Downhole logging was conducted with a limited suite of logging tools, primarily in the upper 295 mbsf.

Site M0080

Site M0080 is located in the Alkyonides Gulf (Figure F1) in the eastern part of the Corinth rift with the aim of testing spatial variation in rift evolution history and to sample earlier phases of rifting. Hole M0080A (water depth of 349 mbsl) was drilled and cored to 534.1 mbsf using the Fugro Corer in push and percussive modes and the FXMCB. Core recovery was 84%. Downhole logging was conducted with a full suite of standard logging tools, with most depth intervals covered.

Lithostratigraphy

The drilled sequences of Expedition 381 comprise an upper unit that records the most recent phase of synrift deformation and deposition (equivalent to seismic Unit 2), a lithostratigraphic unit boundary (of possible unconformable nature in places), and an underlying unit or units (equivalent to seismic Unit 1) that records earlier rift history and represents a variable time period of deposition. The lithostratigraphic units for all sites were defined based on lithologic, micropaleontological, and select physical properties. To characterize the lithostratigraphy, a series of facies associations (FAs) were defined based on physical and biogenic features of the sediment, including bedding and lamination style, grain size, color, and body and trace fossils. The facies associations are defined in Table T3.

Site M0078

The lithostratigraphy of Site M0078 is divided into two units with a boundary at 385.14 mbsf. Unit 1 is divided into 16 subunits (Figure F8) that correlate well with micropaleontological data, which define marine and isolated/semi-isolated intervals that ap-

pear to be primarily controlled by changing eustatic sea level with respect to sills at the entrance to the Corinth basin.

Unit 1 sediments are dominated by detrital clay- and silt-grade carbonate. Background sedimentation consists of hemipelagic and turbiditic muds with occasional thin, coarser (fine silt to medium sand) beds and turbidite-homogeneous mud couplets. Bioturbation is primarily present in the marine subunits. Calcite is most abundant, with common to abundant quartz, feldspars, and micas. Biogenic material is common (in particular in the marine subunits), as are organic components and framboidal pyrite. Well-sorted, silt-sized aragonite needles are dominant in some laminated intervals. Marine subunits in Unit 1 (odd numbers) are dominated by homogeneous to poorly bedded, often greenish gray mud (FA1 and FA6; see Table T3) with some laminated muds (e.g., FA3) and sparse thin silty and sandy beds. Isolated/semi-isolated subunits (even numbers) include laminated muds, thin mud beds, greenish gray mud with homogeneous thick mud beds, and dark gray to black organic-rich beds (FA4, FA3, and FA5) with sparse thin silty and sandy beds. Submillimeter- to millimeter-scale laminations, commonly gray to white, also occur in these isolated/semi-isolated subunits. Throughout Unit 1, interbedded mud-silt and centimeter-thick sand beds are present, but overall sand is minor and decreases with depth (Figure F8).

Unit 2 has a composition similar to that of Unit 1, with well-sorted, very fine silt sized detrital calcite dominant. Unit 2 is composed almost entirely of light gray or buff weakly laminated to homogeneous highly bioturbated mud (FA12; Figure F8). Minor darker gray mud with faint bedding and black laminations associated with organic matter also occurs. The Unit 1/2 boundary is sharp and marked by an abrupt change from laminated greenish gray muds to homogeneous light gray muds downhole.

Site M0079

The lithostratigraphy of Site M0079 is divided into two units with a boundary at 677.23 mbsf (Figure F9). Unit 1 is divided into 16 subunits that correlate well with micropaleontological data, which define marine and isolated/semi-isolated intervals. Unit 1 sediments, as at Site M0078, are dominantly fine grained and carbonate rich. Detrital calcite predominates, with subordinate quartz, feldspar, and phyllosilicates. Biogenic material is common, particularly in the marine subunits. Depositional processes were dominated by fine-grained turbiditic and hemipelagic deposition. Marine subunits in Unit 1 (odd numbers) are moderately to highly bioturbated and dominated by homogeneous to poorly bedded greenish gray muds (FA1 and FA6; see Table T3). Isolated/semi-isolated subunits (even numbers) are dominated by laminated to thinly bedded gray and greenish gray muds, some with black, organic-rich laminations and beds (FA2, FA4, and FA5) with no or sparse bioturbation. Higher energy depositional processes are indicated by intervals of soft-sediment deformation and mud-supported conglomerates (FA13) and sand-homogeneous mud couplets that occur in both marine and isolated/semi-isolated units. Overall occurrence of slumped and mud-supported conglomerates increases with depth in Unit 1, with a particularly thick slumped interval occurring in Subunit 1-11.

Unit 2 has a composition similar to that of Unit 1 and is dominated by light gray to buff weakly laminated to homogeneous highly bioturbated mud (FA12; Figure F9). It is also dominated by fine silt-sized detrital calcite, similar to Site M0078, with lower concentrations of siliciclastic grains compared with Unit 1. In contrast to Site

M0078, Unit 2 contains fining-upward sands (FA10) and large decimeter- to meter-scale slump structures and mud-supported intra-clast conglomerates (FA13).

Site M0080

The lithostratigraphy of Site M0080 is divided into four units with boundaries at 136.96, 256.85, and 458.4 mbsf (Figure F10). Units 1 and 2 are dominated by moderately sorted, silt- to clay-grade calcite. Other minor terrigenous components include quartz, mica, and feldspar mineral grains. Occasionally, both calcite and aragonite occur in equal proportions. Biogenic components and framboidal pyrite are common throughout.

Unit 1 has characteristics similar to those of Unit 1 at Sites M0078 and M0079 and is divided into 11 subunits based on alternations between dominantly bioturbated homogeneous and poorly bedded greenish gray and gray mud (FA1 and FA6) and bedded and laminated mud (FA2, FA3, FA4, and FA5) (Figure F10). These sediments are interpreted as dominantly deep-water turbiditic and hemipelagic deposits. The alternating subunits are interpreted to represent alternating marine (homogeneous mud) and isolated/semi-isolated (bedded and laminated mud) environments, with good correlation with micropaleontology results. Unit 2 is divided into an upper part dominated by light gray bioturbated mud (FA12) and a lower part with greater variability of facies and grain size, including ophiolitic-rich conglomerates, highly bioturbated mudstones with shallow-water foraminifer assemblages, and occasional paleosols. The lower part of this unit reflects a transition downhole in paleoenvironment from subaqueous to subaerial, marking the top of a significant interval of subaerial deposition in Unit 3.

Two main facies associations dominate Unit 3: the upper half has a high proportion of coarse clastic sediments, with clasts including basic/ultrabasic ophiolite, limestone, and chert (FA7), that pass down into distinctive red-brown fine-grained muds and silts of FA8 (Figure F10). The very fine sand to mud fraction commonly contains abundant clay-sized Fe oxides that may be responsible for the reddish brown to pale yellow color of the sediments. The base of the unit comprises a range of facies associations, including shelly bioturbated muds of FA17. The character of the conglomerates and dominance of calcrete soils in Unit 3 suggest an ephemeral alluvial setting subject to a fluctuating water table.

Unit 4 at Site M0080 is dominated by shelly laminated to bedded carbonates (FA15 and FA16) that suggest a reduction in clastic input and most likely formed in a low-energy nearshore setting. The basal two cores of Unit 4 consist of polymict pebble-cobble conglomerates featuring abundant limestone clasts with minor red chert and basic/ultrabasic clasts, reflecting a high-energy alluvial (fan) environment.

Units 3 and 4 include ophiolitic-derived grains and clasts in all grain size fractions but most obviously in the coarser grain size range (sand to pebble grade). Carbonate minerals are most commonly calcite, whereas the ophiolitic-derived mafic sediment grains largely comprise pyroxenes, serpentinized olivine, and plagioclase.

Structural geology

Both natural and drilling-induced deformation were recorded in the cores. Natural faults were distinguished from drilling-induced faulting or other forms of drilling-induced deformation by their planar geometries and lack of influence by proximity to either the core liner or core axis (i.e., by not curving to become parallel to the core

axis, forming conjugate pairs with an intersection at the core axis, or curving into the core liner).

Site M0078

At Site M0078, bedding attitude is horizontal to subhorizontal with local tilting and apparent bedding dips increasing downhole up to 24° (slightly higher than measured dips in coincident seismic reflection data; Figure F5). Small-scale natural faulting was observed sporadically throughout the hole, including frequent normal faults and less common reverse and strike-slip faults. Faulting intensity generally increases with depth but with faulting concentrated in discrete intervals, in particular in the 329–447 mbsf interval around the lithostratigraphic Unit 1/2 boundary. A general lack of faults in the deeper part of Unit 2 may be related to destruction due to rotary drilling-induced biscuiting. Normal fault displacements range from 1 mm to 35 cm, and orientation measurements on selected faults indicate that they may form conjugate sets throughout the core. The sampled normal fault dips show true dips ranging from 42° to 82° with a modal average of 60°–70° and a mean of 66°. The general abundance and geometry of observed small normal faults is in agreement with the overall extensional nature of the rift deformation.

Drilling-induced deformation intensity and style were recorded to determine the state of cores for interpretation and analysis and for potential postexpedition analysis of sediment physical properties variations. A range of drilling-induced structures was observed, including biscuiting, arching bedding, tilted panels, lensing, smearing/flow of sediment along the core lining, voids, and open fractures. In general, drilling-induced deformation increases downhole. Piston coring generated sporadic slight to moderate drilling-induced deformation. Rotary coring from 224 mbsf downhole is associated with a marked increase in intensity (moderate to high) and deformation dominated by biscuiting and inflow of sediment and drilling fluid between biscuits.

Site M0079

Bedding attitude is generally horizontal to subhorizontal despite a gentle increase in dip of reflection horizons in seismic data with depth at Site M0079 (Figure F6). Small-scale natural faulting was observed sporadically throughout the hole, and concentrated faulting was observed in discrete intervals at 48–62, 259–278, 472–548, and 686–698 mbsf. More significant faulting with larger displacements occurs below 547 mbsf. Faulting intensity varies downhole from 0.7 to 10 m⁻¹. All natural faults in Hole M0079A have apparent normal offset, with displacements of 1 mm to >14 cm. Faults sampled for orientation analysis appear to form a conjugate set around an average north–south strike in the core reference frame, but sampling is biased to what is exposed on the split-core face. The abundance and geometry of small normal faults are consistent with those observed at Site M0078 and with the extensional rift deformation.

A wide range of drilling-induced structures was observed, most commonly biscuiting, shear fractures, arching and disturbed bedding, smearing/flow of sediment along the edges of the core, voids, and open fractures; the intensity and style of drilling-induced structures vary downhole. Overall drilling-induced deformation intensity is reduced relative to Hole M0078A (most likely due to changes in drilling and coring methods). Biscuiting is regularly present below 300 mbsf. Below 574 mbsf, cores are more intensely deformed, with biscuiting dominant. Well-developed, drilling-induced shear fracturing is a characteristic feature of Hole M0079A (not observed

in Hole M0078A) and is a regular feature below 276 mbsf. Fractures often form as conjugate pairs typically intersecting in the center of the core or steepening toward the center of the core.

Site M0080

Bedding attitude is generally horizontal to subhorizontal, despite a gentle increase in dip of reflection horizons in seismic data at depth at Site M0080 (Figure F7). Small-scale natural faulting was observed in lithostratigraphic Units 1, 3, and 4, with no faults between 101 and 368 mbsf. The lack of faulting in this interval may be related to lithologic and rheological properties. In Unit 1, faulting intensity varies from 1.4 to 10.5 m⁻¹, and all faults have apparent normal offsets with displacements of 0.2 mm to 3.2 cm. In Units 3 and 4, faulting intensity varies from 0.7 to 4 m⁻¹. Some faults have apparent displacements larger than their length in the core and are characterized by fault gouges and mineralized mirror surfaces with slickenlines. Faults sampled for orientation data illustrate a conjugate fault set striking NNE–SSW in the core reference frame in Unit 1, but sampling is biased to what is exposed on the split-core face. In Units 3 and 4, orientations are more variable, and slickenlines indicate oblique slip and strike-slip motion. The geometries of faults in Unit 1 are consistent with those at Sites M0078 and M0079 and the extensional rift deformation; however, the range of motion senses and geometries in Units 3 and 4 suggest a more complex history of faulting.

A wide range of drilling-induced structures was observed, most commonly biscuiting, shear fractures, arching bedding, smearing/flow of sediment along the edges of the core, and voids; the intensity and style of drilling-induced structures vary downhole. Overall, the intensity of drilling-induced deformation varies, with significant lengths of core with little or none, which may be related to a combination of drilling technique and strength of the materials. Below 15 mbsf, drilling-induced deformation associated with piston coring is pervasive with soupy textures, flow along the core liner and axis, and even complete mobilization and destruction of bedding in some cores. Biscuiting is dominant between 156 and 244 mbsf with the onset of rotary coring and again between 314 and 530 mbsf, where it is associated with intense brecciation between biscuits. Overall, shear fracturing is less common than at Site M0079.

Micropaleontology

Micropaleontological analysis included calcareous nannofossils, marine and nonmarine diatoms, planktonic and benthic foraminifers, and palynomorphs (terrestrial and aquatic pollen and spores, dinoflagellate cysts, green algae coenobia and spores, fungal remains, foraminifer test linings, and microscopic charred particles). The combined examination of microfossil groups in the youngest synrift sediments revealed variations between marine, mixed (marine with nonmarine), nonmarine, and indeterminate (e.g., barren) microfossil assemblages constructed by complex environmental and depositional settings in the Corinth basin; alternating paleoenvironment was particularly evident in the most recent rift phase. Each microfossil group contributes unique information to the regional/basinal paleoenvironmental interpretation. Additionally, calcareous nannofossils contributed to the chronostratigraphic model for the stratigraphic sequence. Diatoms provided critical information about depositional environments in both marine and isolated intervals but especially in isolated intervals. Planktonic and benthic foraminifers were used to interpret the evolution of the paleoceanographic conditions in the basin during marine phases. Palynology

provided a link between the terrestrial and aquatic realms and an assessment of changes in terrestrial paleovegetation and aquatic ecosystems.

Site M0078

The micropaleontology at Site M0078 revealed a high level of complexity both in individual microfossil groups and collectively. In the 16 subunits of lithostratigraphic Unit 1, micropaleontological assemblages alternate primarily between marine and undetermined assemblages but also include several mixed and nonmarine assemblages. Lithostratigraphic Unit 2 is devoid of marine calcareous and siliceous microfossils, containing only nonmarine diatoms and terrestrial and aquatic pollen, dinoflagellate cysts, green algae coenobia and spores, fungal remains, and foraminifer test linings. Calcareous nannofossils were observed in almost all Unit 1 samples but with significantly lower abundances and diversity in the isolated/semi-isolated subunits. In general, *Gephyrocapsa* is the most dominant genus. Late Quaternary age control in Unit 1 is provided loosely by three biostratigraphic events: (1) the last occurrence (LO) of *Pseudoemiliana lacunosa* (0.43 Ma), supported by the co-occurrence with *Umbilicosphaera sibogae*; (2) the first occurrence (FO) of *Emiliana huxleyi* (0.29 Ma); and (3) a crossover in dominance between *E. huxleyi* and *Gephyrocapsa* "small" (<3 μm), documented to be ~70 ka in the Mediterranean Sea (Anthonissen and Ogg, 2012). Because of the punctuated nature of marine environments here, it is important to keep in mind that the precision of these biohorizons is low. Unit 2 is nearly devoid of in situ calcareous nannofossils. Marine diatoms were observed in the majority of the fully marine subunits. Nonmarine diatoms were most commonly observed in the isolated/semi-isolated subunits but were also sometimes observed in low abundance with marine microfossils and were poorly preserved. The assemblages are not diverse and are dominated by species of the *Pontosphaera ocellata* group. The assemblages in the underlying Unit 2 are more diverse but are still dominated by the planktonic *P. ocellata* complex. Benthic and planktonic foraminifers are well preserved but have highly variable abundances and compositions in Unit 1.

Foraminifers tend to be absent or in low abundances in isolated/semi-isolated subunits and abundant to trace in the marine subunits. In the marine subunits, foraminifers reach high abundances, and in general benthic foraminifers tend to be more abundant than planktonic foraminifers. Planktonic and benthic foraminifers are absent from Unit 2 samples. From palynological analysis, the trees versus herbs percentage curve shows alternating periods dominated by forests or herb vegetation that correlate with marine and isolated/semi-isolated intervals, respectively. The interpreted aquatic ecosystem ranges from marine to brackish to evidence for freshwater influx. Highly diverse marine dinoflagellate assemblages correlate with the fully marine intervals, and low dinocyst diversity samples with low salinity indicators suggest deposition under low-salinity (brackish) conditions.

Site M0079

The micropaleontology at Site M0079 revealed a high level of complexity both in individual microfossil groups and collectively, as at Site M0078. In the 16 subunits of lithostratigraphic Unit 1, micropaleontological assemblages alternate primarily between marine and undetermined assemblages but also include some mixed and nonmarine assemblages. Lithostratigraphic Unit 2 is nearly devoid of marine and terrestrial microfossils. Calcareous nannofossils were

observed in almost all Unit 1 samples but with significantly lower abundances and diversity in isolated/semi-isolated subunits. *Gephyrocapsa* is the most dominant species. Late Quaternary age control in Unit 1 is provided loosely by three biostratigraphic events that were also observed at Site M0078: (1) the LO of *P. lacunosa* (0.43 Ma), (2) the FO of *E. huxleyi* (0.29 Ma), and (3) a crossover in dominance between *E. huxleyi* and *Gephyrocapsa* “small” (<3 µm). Because of the punctuated nature of marine environments here, it is important to bear in mind that the precision of these biohorizons is low. Unit 2 is completely devoid of in situ calcareous nannofossils. As at Site M0078, marine diatoms were observed in the majority of the fully marine subunits. Nonmarine diatoms were most commonly observed in the isolated/semi-isolated subunits, typically in combination with low abundances of marine microfossils. On occasion, nonmarine diatoms were observed in low abundance in marine intervals; however, because of poor preservation, they are not interpreted to be in situ. The nonmarine diatom assemblages are dominated by several morphotypes of the *P. ocellata* complex. Benthic and planktonic foraminifers are well preserved but have highly variable abundances and compositions in Unit 1. Eight intervals with relatively high abundances of benthic and/or planktonic foraminifer species in Unit 1 suggest the prevalence of marine conditions. In these intervals, benthic foraminifer abundance is generally higher than that of planktonic foraminifers. Foraminifers tend to be absent or in low abundances in isolated/semi-isolated subunits, although intervals with higher foraminifer abundance were also observed. Planktonic and benthic foraminifers are absent from Unit 2 samples. The majority of the pollen assemblages corresponding to marine intervals in Unit 1 are characterized by high tree abundances, suggesting the occurrence of forested landscapes in the surroundings of the Gulf of Corinth, whereas in pollen assemblages corresponding to isolated/semi-isolated intervals, herb and tree abundances are nearly equal. As at Site M0078, dinoflagellate assemblages show alternating periods of marine and brackish paleoenvironments correlating with marine and isolated/semi-isolated intervals, respectively.

Site M0080

At Site M0080, the microfossil assemblages in lithostratigraphic Unit 1 indicate alternation primarily between marine and undetermined/barren assemblages but also include a few mixed and nonmarine assemblages toward the base of the unit. Unit 2 alternates between nonmarine and undetermined/barren assemblages. Unit 3 is devoid of microfossils except palynomorphs because it is almost entirely terrestrial. Unit 4 is nearly devoid of the microfossil groups analyzed, with the exception of three samples that contain calcareous nannofossils in very low concentrations. Calcareous nannofossils similar to those observed at Sites M0078 and M0079 were observed in all marine intervals in Unit 1. Late Quaternary age control in Unit 1 is loosely provided by two biohorizons: (1) the crossover in dominance between *E. huxleyi* and *Gephyrocapsa* “small” (<3 µm) and (2) the FO of *E. huxleyi*. As at Sites M0078 and M0079, the true FO of *E. huxleyi* was probably not observed. Units 2 and 3 are devoid of in situ calcareous nannofossils, and nannofossils are rarely present in Unit 4, where their implications for age are being investigated. Initial investigations suggest marine diatoms are present in significantly lower abundances than at Sites M0078 and M0079. The nonmarine diatom assemblages show better preservation and greater diversity of benthic taxa, indicating a shallower environment compared with the other two sites. Benthic and

planktonic foraminifers are present only in Units 1 and 2, with highly variable abundances and compositions. Planktonic foraminifers similar to those observed at Sites M0078 and M0079 were observed in all marine intervals in Hole M0080A. The benthic foraminifer assemblages in the lower part of Unit 1 and in Unit 2 imply shallow-marine depositional environments. Pollen assemblages in Units 1 and 2 corresponding to interpreted marine intervals show high tree abundances, suggesting the occurrence of a forested landscape surrounding the Alkyonides Gulf, whereas in isolated/semi-isolated intervals, herb and tree abundances are nearly equal. Dinoflagellate assemblages indicating marine and brackish paleoenvironments were observed in Units 1 and 2, whereas Units 3 and 4 were devoid of dinocysts.

Geochemistry

Pore water was collected from core samples offshore using Rhizons and squeeze cakes. Offshore, these samples were analyzed for alkalinity, ammonium, pH, and salinity. During the OSP, a combination of methods was applied to pore water samples to measure anions, cations, phosphate, and dissolved inorganic carbon (DIC). Solid samples were selected and processed during the OSP and were measured for X-ray fluorescence (XRF) elemental composition, X-ray diffraction (XRD; results were incorporated into **Lithostratigraphy**), total carbon (TC) and total organic carbon (TOC).

Site M0078

At Site M0078, 82 pore water samples were analyzed from Holes M0078A and M0078B, and 127 bulk sediment samples were processed during the OSP. Pore water and solid-phase chemical results follow very similar trends in Holes M0078A and M0078B. Pore water composition in the uppermost 30–50 mbsf at Site M0078 reflects a diffusion profile of dissolved elements from the water column into the sediments (sodium, chloride, and sulfate) and ions produced during the degradation of organic matter (ammonium, bicarbonate, phosphate, iron, and manganese) diffusing from the sediments into the water column. Comparison of salinity values to those of sodium and chloride indicate that the major salt contributing to the pore water is sodium chloride. Significant changes between the pore water above and below the lithostratigraphic Unit 1/2 boundary were observed; higher concentrations of sodium and chloride and ions associated with carbonates (calcium, magnesium, and strontium) were observed below the boundary. Changes in pore water composition below the Unit 1/2 boundary may reflect the change in sediment composition, which is evident from the elemental composition of the solid sediment. Although solid sediment samples are carbonate rich throughout Hole M0078A, below the Unit 1/2 boundary an increase in the dominance of carbonate is clear from higher calcium concentrations. Organic carbon is low throughout Site M0078, ranging from 0.07 to 0.89 wt%.

Site M0079

At Site M0079, 77 pore water samples were analyzed, and 111 bulk sediment samples were processed during the OSP. From the seafloor to approximately 50 mbsf, pore water composition shows decreasing salinity (from 38.17 to 10.48) alongside decreasing pore fluid sodium, chloride, and sulfate concentrations, reflecting a diffusion of ions from the seawater into the sediment. Dissolved chloride ranges between 7.82 and 610.49 mM, and dissolved sodium varies from 51.65 to 541.73 mM; their highest values are in the upper 0.5 mbsf at the sediment/water interface.

Iron, which varies between 0 and 71.52 μM , and manganese, which ranges from 0 to 220.63 μM , both increase in the uppermost 9 mbsf, most likely due to generation of these ions during microbial oxidation of organic matter. Other ions generated during the degradation of organic matter (ammonium, bicarbonate, and phosphate) also show this increase in the uppermost part of the hole but fluctuate with depth, reflecting the complex nature of the geochemical environment. Ions commonly associated with carbonates (calcium [mean = 3.82 mM], magnesium [mean = 17.41 mM], and strontium [mean = 0.11 mM]) also vary with depth and, similar to Hole M0078A, increase at the base of Hole M0079A. These observations are in agreement with the solid sample analyses.

Analysis of solid sediment samples (total inorganic carbon [TIC] and calcium) suggests that the sediment is predominantly composed of carbonate, which generally increases with depth (Ca = 175.0–228.0 g/kg; TIC = 3.95–10.52 wt%). Elements associated with detrital material (silicon, aluminum, zircon, and potassium), in contrast, decrease with depth.

Site M0080

At Site M0080, 62 pore water samples were analyzed, and 68 bulk sediment samples were processed during the OSP. Pore water profiles in the uppermost section of Hole M0080A show changes that most likely reflect diffusion profiles. Decreases in salinity from close to seawater values (35.74) to much lower values (12.38) at 49 mbsf, along with decreases in sodium, chloride and sulfate concentrations, are likely linked to diffusion from seawater into the sediment. The highest concentrations of dissolved iron and manganese (as high as 166.74 and 31.45 μM , respectively) at the top of the hole decrease to relatively stable state concentrations below around 30 mbsf. This trend is likely due to generation of these dissolved ions during oxidation of organic matter and diffusion into the water column. Concentrations of other ions linked to organic matter degradation (ammonium, phosphate, alkalinity, and DIC) also increase in the uppermost 20 mbsf (with maxima of 2.1 mM, 21.44 μM , 13.87 mM, and 12.59 mM, respectively). Below this depth, these ions continue to be present in variable concentrations, possibly relating to various loci of organic matter degradation.

Below the lithostratigraphic Unit 2/3 boundary, ions relating to organic matter degradation are generally present in low concentrations, whereas ions related to marine seawater appear to be high, comparable to modern day local seawater. Calcium and magnesium ion concentrations, which are typically related to carbonate, also increase in Unit 3. Average calcium and magnesium ion concentrations are 8.16 and 38.86 mM, respectively, throughout the hole but reach maxima of 34.65 and 86.85 mM, respectively, in Unit 3.

Bulk geochemical results from solid sample analysis indicate that lithostratigraphic Units 1, 2, and 4 are dominated by calcium carbonate, with inorganic carbon averaging 8.34 wt% and calcium averaging 237.77 g/kg. In Unit 3, silicon dominates with an average of 172.68 g/kg compared with 83.63 g/kg in Units 1, 2, and 4. This switch in dominance, alongside higher values of aluminum, potassium, rubidium, and zirconium, suggests a change to more siliclastic sediment in Unit 3. Organic carbon content is low throughout, averaging 0.24 wt%, and is lowest in Unit 3 (average = 0.06 wt%).

Physical properties

Physical properties data acquired offshore and onshore on whole cores, split cores, and discrete samples exhibit coherent variations with depth and between different lithologies. Shear strength

was estimated with handheld penetrometer measurements on whole cores and in situ cone penetration tests offshore and from fall cone and shear vane tests on split cores during the OSP. MSCL density data were acquired on whole cores offshore, and moisture and density (MAD) density and porosity were measured on discrete samples during the OSP. MSCL magnetic susceptibility, resistivity, and natural gamma ray (NGR) data were acquired offshore on whole cores, and color reflectance data were acquired on split cores during the OSP. Attempts were made to collect *P*-wave velocity data on whole cores, half cores, and discrete samples. At Sites M0078 and M0079, reliable velocity measurements were only obtained in restricted intervals, primarily in the upper parts of the core, but reliable results were obtained for a large part of Site M0080. Between the offshore phase and the OSP, thermal conductivity measurements were conducted on whole cores prior to splitting.

Site M0078

At Site M0078, MAD, MSCL density, MSCL resistivity, and shear strength data indicate increases in sediment density and strength and a reduction in porosity with depth, consistent with compaction (Figure F8). Sharp increases in density and shear strength were observed at 225 mbsf, near the transition to rotary coring. Overall, low NGR values at Site M0078 indicate low potassium (K), uranium (U), and thorium (Th) concentrations.

Physical properties vary between the two defined lithostratigraphic units. In Unit 1, physical properties show clear variation between the marine and isolated/semi-isolated subunits. Marine subunits (odd numbers) are characterized by higher NGR values and lower and less scattered magnetic susceptibility values than isolated/semi-isolated subunits (even numbers; Figure F8). Lower density values are commonly associated with marine subunits and/or with transitions from these subunits into those above and below. Marine subunits have lower mean L^* and a^* values and higher mean b^* values compared with the means for the hole. Unit 2 is characterized by low and highly variable NGR values, scattered magnetic susceptibility values, low thermal conductivity, and lighter colors, resulting in higher mean L^* and a^* values and lower b^* values from color reflectance data. Density values are less scattered in Unit 2 but show in-core trends in MSCL data related to coring and drilling.

Site M0079

Overall, as at Site M0078, MAD, MSCL density, MSCL resistivity, and shear strength data at Site M0079 indicate increases in sediment density and strength and a reduction in porosity with depth, consistent with compaction (Figure F9). However, low shear strength, density, and velocity values and high porosity values in the upper ~200 mbsf suggest relatively little compaction in this interval. Comparison between *P*-wave velocity values from discrete measurements, those from the downhole logging data, and those predicted by core-log-seismic integration (CLSI) suggests that velocity values in the upper ~225 mbsf are realistic, but that velocity values below this depth are anomalously low.

Also similar to Hole M0078A, significant variations in Hole M0079A were observed in many physical properties between the marine and isolated/semi-isolated subunits in Unit 1. Marine subunits are characterized by higher NGR values and lower and less scattered magnetic susceptibility values than isolated/semi-isolated subunits (Figure F9). Lower density values are commonly associated with marine subunits and/or with transitions at the boundaries of these subunits. Conversely, shear strength and velocity appear to increase in some marine subunits. Marine subunits have lower

mean L^* and a^* values and higher mean b^* values compared with means for the hole from color reflectance data.

The lithostratigraphic Unit 1/2 boundary does not have a clear expression in physical properties measurements.

Site M0080

Physical properties from Hole M0080A cores show more variability than at Sites M0078 and M0079, reflecting the greater diversity of depositional environments and lithologies encountered. Most lithostratigraphic unit boundaries have a clear signature in the physical properties data. A change was also observed in most physical properties data sets at the boundary between Subunits 3-1 and 3-2 at ~350 mbsf. Density values increase steadily with depth, consistent with compaction and strengthening (Figure F10). Resistivity shows slightly more complex variation with depth, with a pronounced increase in values downhole at the Unit 3/4 boundary.

Variations in physical properties reflecting environmental variation in Unit 1 were observed, as at Sites M0078 and M0079. In Unit 1, density and magnetic susceptibility increase and porosity and NGR decrease in isolated/semi-isolated intervals relative to the marine intervals. Marine subunits have lower mean L^* and a^* values and higher mean b^* values compared with means for the hole from color reflectance data. Density, color reflectance, and porosity values become more scattered in the lower part of Unit 2 and transitioning into Unit 3. NGR decreases and then increases in Unit 3, followed by a sharp decrease into Unit 4 (Figure F10). Magnetic susceptibility increases in Unit 3, with a slight decrease with depth and a sharp reduction into Unit 4. These trends are thought to reflect the varied composition of the changing subaqueous and subaerial sequences in these units (see [Lithostratigraphy](#)).

Velocity data from discrete measurements in Units 1 and 2 are relatively low, but some values are consistent with sonic data acquired by downhole logging. In Units 3 and 4, both discrete and MSCL P -wave data appear to be more reliable. Velocity values average 2000 m/s in the lower part of Unit 3. Unit 4 is characterized by increased velocity values but with variations between the two core velocity data sets (2000–3000 m/s on the MSCL and 2000–3500 m/s on discrete samples).

Paleomagnetism

Site M0078

Magnetic susceptibility was measured on 500 samples from Holes M0078A and M0078B, and the results show a good match with MSCL magnetic susceptibility. Above ~300 mbsf, magnetic susceptibility variations are relatively small and exhibit different patterns in marine and isolated/semi-isolated subunits. Much higher variability in magnetic susceptibility was observed below ~300 mbsf. Overall, magnetic susceptibility and natural remanent magnetization (NRM) exhibit similar patterns with depth, suggesting that variations in susceptibility are primarily controlled by the concentration of magnetic minerals.

Thermal variation in magnetic susceptibility was determined on five representative samples at the University of Hawaii prior to the OSP. Most samples show a primary Curie temperature of 518°–577°C, indicating the occurrence of Ti-poor titanomagnetite, although a couple of lower Curie temperatures may indicate the occurrence of greigite.

The direction and intensity of NRM were also determined on 500 samples from Holes M0078A and M0078B. The inclination values are dominantly positive (normal polarity) in Unit 1, which may

correspond to the Brunhes Normal Chron (0–0.773 Ma). Some anomalous low inclinations in this upper interval may represent excursions of the geomagnetic field in the Brunhes Chron. Below the transition from Unit 1 to 2, inclination values are dominantly negative (reversed polarity), although several samples with normal polarity are also present.

Site M0079

Magnetic susceptibility was measured on 532 samples from Hole M0079A, and the results show a good match with MSCL magnetic susceptibility. Above ~540 mbsf, magnetic susceptibility variations are relatively small and exhibit different patterns in marine and isolated/semi-isolated subunits. Much higher variability in magnetic susceptibility was observed below ~540 mbsf. Overall, magnetic susceptibility and NRM exhibit similar patterns with depth, suggesting that variations in susceptibility are primarily controlled by the concentration of magnetic minerals.

Thermal variation in magnetic susceptibility was determined on eight representative samples at the University of Hawaii prior to the OSP. The results of the thermomagnetic experiments reveal a wide range of Curie temperatures between 364° and 595°C. However, most of the samples show a primary Curie temperature between 502° and 585°C, which is typical of Ti-poor titanomagnetite. Other Curie temperatures between 364° and 486°C suggest the occurrence of iron sulfides (likely greigite) or Ti-rich titanomagnetite.

The direction and intensity of NRM were also determined on 532 samples from Hole M0079A. The inclination values are dominantly positive (normal polarity) in Unit 1, with the exception of two samples that show a negative inclination (reversed polarity). This uppermost interval may represent the Brunhes Normal Chron, with the two reversed polarity samples possibly corresponding to excursions of the geomagnetic field. Inclination values show a wider variability from negative to positive below this depth and require further postexpedition analysis.

Site M0080

Magnetic susceptibility was measured on 379 samples from Hole M0080A, and the results show a good match with MSCL susceptibility. Above ~250 mbsf, magnetic susceptibility variations are relatively small. A much higher variability, with overall higher values of susceptibility, was observed between ~250 and ~460 mbsf, likely related to the occurrence of mafic ophiolitic clasts in Unit 3. Magnetic susceptibility and NRM exhibit similar patterns with depth, suggesting that variations in susceptibility are primarily controlled by the concentration of magnetic minerals. The results of the thermomagnetic experiments reveal a wide range of Curie temperatures between 116° and 646°C, indicating the occurrence of Ti-rich titanomagnetite, iron sulfides (likely greigite), and likely oxidized titanomagnetite (i.e., titanomaghemite).

The direction and intensity of NRM were also determined on 379 samples from Hole M0080A. The inclination values are dominantly positive (normal polarity) in Units 1 and 2 and the uppermost part of Unit 3, with six samples showing a negative inclination (reversed polarity). At greater depths, samples have a dominantly negative inclination (reversed polarity) that become positive again toward the bottom of the hole. The polarity transition observed in Unit 3 corresponds to the Brunhes/Matuyama boundary (0.773 Ma). The reversed polarity intervals observed in the uppermost normal polarity interval may represent excursions of the geomagnetic field during the Brunhes Normal Chron.

Downhole logging

Site M0079

Downhole logging data were collected through pipe (gamma ray) from the bottom of Hole M0079A to the seafloor and in the upper part of the open hole with logs recording magnetic susceptibility and conductivity (~297 to ~50 m wireline log depth below seafloor [WSF]), sonic velocity (~230 to ~50 m WSF), and dual resistivity (~290–50 m WSF). Gamma ray values, even though measured through the pipe, compare well with MSCL data collected on cores. The overall trend shows some correspondence to the marine and isolated/semi-isolated intervals. The slumped interval described in the deeper part of Unit 1 (484.48–506.4 mbsf; see **Lithostratigraphy**) is associated with a clear drop in gamma ray counts. Resistivity values derived from the conductivity data (magnetic susceptibility and conductivity tool) and collected with the dual resistivity log compare well with each other and with MSCL resistivity data acquired on cores, and the values indicate low resistivity in the formation (typically <5 Ω m). Trends in the magnetic susceptibility log acquired downhole mirror those from MSCL data on cores, with a clear variation associated with changing basin environment: magnetic susceptibility tends to be lower in marine intervals/subunits and higher and more scattered in the isolated/semi-isolated intervals/subunits. Sonic data suggest low velocity, typically between 1500 and 1700 m/s from 50 to 190 m WSF and increasing to values as high as ~1900 m/s from 190 to 230 m WSF.

Site M0080

Hole M0080A logging operations were very successful, with most of the hole (0 to ~530 mbsf) covered with a suite of standard logging tools: spectral gamma ray through pipe and magnetic susceptibility and conductivity, dual induction resistivity, sonic, and spectral gamma ray in the open hole. Spectral gamma ray data were acquired through the pipe from the bottom of the hole to the seafloor and in the open hole principally from ~370 to 50 m WSF. Magnetic susceptibility and conductivity data cover most of the hole, with gaps from ~220 to ~230 m WSF and at 430 m WSF. Dual induction (resistivity) data cover the hole from ~370 to 50 m WSF, with a gap from ~220 to ~230 m WSF. Sonic data cover from the bottom of the hole to 50 m WSF, with gaps from ~430 to ~370 and from ~230 to ~220 m WSF.

The collected logs reflect the main lithostratigraphic units identified in Hole M0080A. In particular, magnetic susceptibility log data clearly respond to the changing depositional environments and potentially sediment composition. Unit 1 is characterized by gamma ray counts of 50–100 counts/s, low magnetic susceptibility values, and relatively low velocity values between 1500 and 1600 m/s, consistent with some of the discrete velocity measurements. Gamma ray increases in marine subunits, and magnetic susceptibility shows locally higher values in the isolated/semi-isolated subunits of Unit 1. In Unit 2, the gamma ray counts are lower than in Unit 1 and magnetic susceptibility remains low with local increases in Subunits 1-4 and 1-5. Velocity values increase to 1700–2000 m/s in Unit 2. Magnetic susceptibility increases significantly in Unit 3, associated with increased scattering. Similar scattering was observed in the resistivity data, and sonic velocity increases to values >2000 m/s. Data in this unit may be affected by poorer and variable borehole conditions. At the boundary between Subunits 3-1 and 3-2, magnetic susceptibility decreases, gamma ray increases, and resistivity and sonic velocity sharply increase. In Unit 4, gamma ray (through pipe) drops again to reach values <20 counts/s, magnetic

susceptibility remains low with little variation, and sonic velocity increases abruptly to values close to 3000 m/s.

Velocity data acquired on whole-round cores (MSCL) and discrete samples and from downhole logs show similar trends, but values differ slightly in some parts of the hole. In particular, in the deeper part of the hole (Unit 4) MSCL data indicate velocity values of 2000–2500 m/s, sonic data values are between 2500 and 3500 m/s and higher, and discrete core measurement values sit between these two data sets.

Core-log-seismic integration

The goal of CLSI during Expedition 381 was to tie data and observations from each of the sites to the extensive seismic reflection database available in the Gulf of Corinth (e.g., Sachpazi et al., 2003; Zelt et al., 2004; Taylor et al., 2011; McNeill et al., 2005; Bell et al., 2008, 2009; Lykousis et al., 2007; Sakellariou et al., 2007; Collier et al., 2000; Leeder et al., 2002, 2005; Stefatos et al., 2002; Charalampakis et al., 2014; Nixon et al., 2016) (e.g., Figure F3). Synthetic seismograms were calculated with MSCL and MAD density and, where available, with velocity information from downhole logging, core physical properties, or existing pre-expedition velocity profiles derived from seismic data.

Site M0078

Synthetic seismograms for Site M0078 (Figure F5) were calculated from MSCL density data from Holes M0078A and M0078B and a velocity function estimated from seismic data before the expedition. Unfortunately, neither core MSCL nor discrete V_p measurements produced reliable velocity data for Site M0078. Nonetheless, the synthetic seismograms can be reliably tied to the seismic data using the pre-expedition velocity function. Minor adjustments to the velocity function were made to match prominent reflections in the synthetic seismogram to those in the coincident seismic data. Above 250 mbsf, the main high-reflectivity horizons in lithostratigraphic Unit 1 (seismic Unit 2) correspond to marine subunits, confirming the interpretations of Nixon et al. (2016) and other previous authors. However, the marine intervals are sometimes thinner than estimated from the reflection data prior to the expedition. In the lower part of Unit 1 (below ~250 mbsf), correlating seismic reflectors with subunit boundaries becomes more challenging because this part of the section is condensed and parts of the section may be missing. In this depth range, observed marine and isolated/semi-isolated subunits sometimes correspond to the seismic phases but sometimes differ. The lower reflectivity sequences of lithostratigraphic Unit 2 (seismic Unit 1; Figure F5) proved to be more challenging to match to seismic reflection data due to the lack of impedance contrasts in the core and seismic records. However, at least two low-reflectivity horizons in Unit 2 can be potentially traced in the synthetic seismogram and tied to seismic data.

Site M0079

MSCL density data were combined with a velocity function created from discrete velocity values and sonic data from downhole logging in the upper part of Hole M0079A and a velocity function based on preliminary offshore CLSI in the lower part of the hole to calculate synthetic seismograms. A comparison of all available velocity information indicates that the upper ~200 mbsf is characterized by relatively low velocity values that suggest limited compaction, consistent with other physical properties. Further minor adjustments to the velocity function were made to match prom-

inent reflections in the synthetic seismogram to those in the coincident seismic data. Synthetic seismograms exhibit patterns of high and low reflectivity similar to those observed in seismic data crossing the site (Figure F6). Intervals of high reflectivity in synthetic seismograms correspond to marine subunits from lithostratigraphic Unit 1, confirming the interpretations of Nixon et al. (2016) and previous authors. In detail, CLSI demonstrates that the tops of marine intervals correspond to the onsets of high-reflectivity intervals. In the lower part of Unit 1, the relationship between bright reflections and marine subunits is more complex, likely owing to the small thicknesses of marine subunits and intervals in this part of the hole. The deepest reflection, interpreted as the unit boundary in seismic data, may in fact correspond to the deepest marine interval of lithostratigraphic Unit 1.

Site M0080

For Site M0080, MSCL density data were combined with a velocity function created from discrete velocity values, sonic data from downhole logging, and velocity values from offshore MSCL data to calculate synthetic seismograms. A comparison of all available velocity information indicates that the upper ~140 mbsf is characterized by relatively low velocity values that suggest limited compaction, consistent with other physical properties. From ~150 to ~450 mbsf, an increase in velocity corresponds, on average, to the velocity function estimated from seismic data before the expedition. Below ~450 mbsf, there is a significant difference in average MSCL velocity values and the downhole logging velocity values, with the former suggesting a lower range of ~2000–2500 m/s and the latter varying from ~2500 to 3500 m/s. Both velocity scenarios were utilized for synthetic seismogram generation to determine their sensitivity to uncertainty in the input velocity profile.

Synthetic seismograms at Site M0080 match the coincident seismic data remarkably well, but the correlation in Unit 4 is less clear. The four lithostratigraphic units identified from the cores have visibly different expressions in the seismic data around the site (Figure F7). Lithostratigraphic Unit 1, a succession of relatively thin marine and isolated/semi-isolated subunits, exhibits a series of continuous reflectors with a very pronounced positive phase, likely produced by the change to lower density in the marine intervals (from other physical properties data sets). Select subunit boundaries can be reliably traced from the cores to the seismic data. Lithostratigraphic Unit 2 is characterized by a series of continuous reflectors with equally pronounced positive and negative phases. Lithostratigraphic Unit 3 has a more complex reflectivity signature characterized by discontinuous reflectors and some gaps in reflectivity, corresponding to the conglomerates in Subunit 3-1 and potential faults at the base of Subunit 3-2. Below ~450 mbsf, the synthetic seismogram and its correlation with lithostratigraphic Unit 4 varies significantly depending on the input velocity model. For the case of lower input velocity values derived from MSCL data, the top and bottom of Unit 4 are marked by two distinct reflectors, the shallower of which was previously attributed to the top of acoustic basement (Nixon et al., 2016) but could now be interpreted as the transition into basal conglomerates. Alternatively, using the higher velocity values derived from the downhole log data, the whole of Unit 4 maps onto the upper of these two reflectors, and subunit boundaries in Unit 4 cannot be resolved. In this case, the reflector interpreted as the top of acoustic basement would be intersected at the very bottom of Hole M0080A. Based on the properties of the cored materials, the latter interpretation is favored, but further work will be required to distinguish between these two end-members.

Preliminary scientific assessment

The overarching objective of Expedition 381 was to drill, sample, and analyze the synrift sedimentary sequence that records an extended period of the early stage continental rifting process in the Corinth rift, Greece. This is the first time a record of this length and resolution has been recovered in an active rift system. In the Corinth rift, part of the rift depositional record is preserved onshore, but the most recent sequence is only present offshore. Onshore, only limited dating of the sedimentary sequence has been possible; therefore, there is little constraint on geological timing and the rates of processes. Obtaining this record makes it possible to develop the chronostratigraphy, determine the environment of the basin through its rift development history, quantify changes in depositional processes and sediment flux in the basin, and determine the rates and timings of rift and fault development, fault slip, and fault activity history.

Expedition 381 was extremely successful. The drilling and coring objectives were almost completely achieved, and a total of 1645 m of core was recovered from three sites over a 1905 m cored interval. At Site M0078, the borehole depth was shortened slightly due to projected time constraints; therefore, an intended part of the older synrift section was not recovered. At Site M0080, the drilling target was to reach acoustic basement (the older sedimentary sequences underlying the synrift sequence). Basal conglomerates interpreted to immediately overlie basement were recovered, but there was insufficient time to continue to basement itself. Due to hole stability problems and the loss of tools in one hole, only partial logging of the three sites was conducted. At Site M0078, logging operations were conducted, but data are probably not usable. At Site M0079, a limited suite of logging tools were deployed, primarily only in the upper ~295 m of the hole. At Site M0080, a full suite of standard logging tools were used to collect data through almost the entire borehole. In spite of these (relatively minor) changes to the operational program, the combined coring and logging data sets collected will fully enable us to address the objectives of the expedition. Core recovery was excellent (average 86%), and core quality is good overall. Changes to coring and drilling methods during the expedition significantly improved subsequent core quality and increased rates of progress, enabling the three sites to be completed very nearly as planned in the time available.

The potential range of scientific applications for this unique data set is very large, encompassing tectonics, sedimentary processes, paleoenvironment, paleoclimate, paleoecology, geochemistry, and geohazards. We anticipate exciting and important results from both the postexpedition research and from research endeavors beyond the science party for many years to come.

Active rift sedimentary processes

The three drill sites of Expedition 381 capture a long and high-resolution record of sedimentation in the center of the Gulf of Corinth and Alkyonides Gulf, with primarily fine grained, distal sediment gravity flow and hemipelagic deposits. The core materials show a clear link to the changing environment of the basin in the most recent synrift succession, namely an alternation between a marine environment during global sea level highstands and an isolated/semi-isolated environment during global sea level lowstands. In the marine intervals, sediments are predominantly homogeneous bioturbated muddy sediments with a marine biogenic assemblage. In the isolated/semi-isolated intervals, sediments tend to exhibit clearer bedding and fine-scale lamination, with coarser laminations

and beds apparently more pronounced. Sediment composition, primarily carbonate, shows a clear correlation with onshore drainages and sediment sources, and grain analyses will be used in post-expedition research to assess changes in provenance. Organic components are common in the sediments, possibly with both marine and terrestrial sources, and these components in turn affect the geochemistry of the sediments and pore waters. In the deeper and earlier rift sequences of the sites in the central gulf (Sites M0078 and M0079; Figure F1), sediments become more homogeneous and lack the clear cyclical signature related to the changing environment of the basin driven by global sea level seen in the overlying sequence. Slump and debris flow deposits appear to be more common at depth in the sequence, in particular at Site M0079, and may reflect a change in rift faulting and activity and/or sediment flux.

In the Alkyonides Gulf at Site M0080 (Figure F1), many differences are seen in the sedimentary sequence compared with sites in the central gulf (Sites M0078 and M0079). Some of these differences may reflect the smaller drainage systems feeding the basin, the shallower water depth of the site, and/or closer proximity to the shoreline. At depth at Site M0080, terrestrial alluvial–fluvial sequences and deposits indicative of a shallow ephemeral basin fluctuating between a subaqueous and subaerial environment are preserved. These deposits predate the most recent phase of deeper water deposition affected by changing global sea level. The exact age of these older deposits is not yet clear, but they may include a record of an earlier phase of Corinth rifting than that penetrated by the boreholes in the central gulf. Correlation of the earliest deposits at all three sites with the onshore exhumed synrift sequences will be a crucial element of postexpedition research to generate a complete history of Corinth rift evolution and deposition and to identify any along-axis variations in rift evolutionary history.

Paleoenvironment of the Corinth rift basin

Sediments from the most recent rift phase reveal substantial temporal variations in paleoenvironment in the Gulf of Corinth that appear to be driven by sea level fluctuations with respect to the topographic sills bounding this semi-isolated basin and the supply of riverine water to the basin. These changes are manifest in varying microfossil assemblages, sediment lithology, and the chemistry of the basin sediments and pore fluids. During marine periods when the gulf was connected to the global oceans, full suites of marine microfossils were observed, including combinations of benthic and planktonic foraminifers, marine diatoms, calcareous nannofossils, and marine dinoflagellate cysts; however, the abundance and diversity of microfossil groups vary between sites and with time. During isolated/semi-isolated periods when the gulf appears to have been cut off from the global ocean, microfossil assemblages are often complex, suggesting multifaceted paleoenvironmental conditions. The transitions between the marine and isolated/semi-isolated intervals expressed in the micropaleontological and sedimentary record are particularly complex and varied in their length and character. Pollen analysis of the deposits also provides a link between the terrestrial and aquatic environments during this time. The sea level–driven paleoenvironmental change in the late Quaternary basin is also recorded in the lithology and geochemistry of the most recent synrift sediments. The volume and mode of sediment delivery into the rift basin appear to change between marine and isolated/semi-isolated intervals. Variations in the geochemistry of the sediments and pore fluids were also observed over this part of the drilled interval, with apparent links to paleoenvironmental changes.

At greater depths in the boreholes, older parts of the synrift sedimentary fill appear to be dominantly nonmarine. In the central gulf (Sites M0078 and M0079), the gulf appears to have been primarily isolated during this earlier phase. Although extended intervals are devoid of microfossils, likely as a result of preservation (e.g., dissolution, scavenging, etc.), significant bioturbation was observed; therefore, the environmental conditions in these periods are less clear. In the Alkyonides Gulf (Site M0080), the recovered synrift sediments from earlier phases of basin development indicate both terrestrial and subaqueous conditions.

Further postexpedition research and integration of micropaleontological, sedimentological, and geochemical observations and analyses will be needed to more fully understand the complex changes in paleoenvironment over the history of the Corinth rift and how these relate to its tectonic and climatic evolution. Comparisons with other basins with varying paleoenvironments, such as the Marmara Sea and Black Sea, will form part of this process. The Corinth rift cores will also provide a new, long Quaternary record of Mediterranean-type climate in the region, complementing long records farther north in the southern Balkans–Greece, such as from Lake Ohrid, Lake Kopais, Lake Ioannina, Tenaghi Philippon (e.g., Tzedakis et al., 2009; Sadori et al., 2016), and elsewhere in the Mediterranean Sea.

Chronostratigraphy

One of the primary objectives of Expedition 381 was to obtain age constraints on synrift sediments that can be used to quantify rates of tectonic and sedimentary processes at high temporal resolution in this young and active rift. Shipboard characterization of the recovered cores indicates that this objective will be achievable by using a suite of complementary dating and paleoenvironmental characterization methods, although this process will take time and will be challenging. Shipboard analyses have already yielded important age constraints that will be greatly expanded by post-expedition research efforts.

Shipboard efforts included biostratigraphy, magnetostratigraphy, and, less directly, identification of alternating basin conditions linked to past sea level fluctuations and glacial–interglacial cycles. Two key calcareous nannofossil markers were observed in the sedimentary record of the most recent rifting phase: *E. huxleyi* (FO at 0.29 Ma) and *P. lacunosa* (LO at 0.43 Ma). However, because the basin alternates between marine and isolated conditions and thus does not possess a continuous record of marine microfossils, interpreting these microfossil observations must be undertaken with care. Magnetostratigraphy provides baseline chronological ties for the drilled section, including probable identification of the Brunhes/Matuyama boundary at all sites and potential correlations with other earlier chrons. With further postexpedition research, the opportunity to identify excursions of the geomagnetic field and to develop and correlate with the global RPI record should further improve the resolution of the chronostratigraphy. Finally, pinpointing changes in basin paleoenvironment linked to glacial–interglacial cycles also provides indirect age constraints. These data indicate that the most recent phase of rift deformation is late Quaternary and that pre-expedition correlations with glacial–interglacial cycles are broadly correct. The penultimate phase of rift deformation also appears to be Quaternary in age, but further analysis is required to pinpoint ages more precisely and to examine any spatial variations in the extent of the rift history preserved in the gulf and sampled at all three sites.

The cores clearly contain a rich trove of material that can be used to provide further age constraints. To develop a final age model for each site, shipboard results will be complemented by a series of postexpedition research efforts, including radiocarbon dating of the youngest sediments, stable isotope analyses from the marine intervals, magnetic RPI, and tephrochronology. The results will be crucial for studies of rift evolution, sedimentary processes, and paleoenvironment.

Structure and deformation

The three drill sites were purposely located away from major seismic-scale faulting to maximize recovery of a complete stratigraphic sequence and to avoid the problems of drilling through faults. However, small-scale deformation, primarily compatible with the present-day extensional regime, was observed in the cored sequence at all three sites. Deformation tends to be more common with depth, probably reflecting the syntectonic nature of the sedimentary sequence. Fault structures are most common in the deeper part of Site M0080 in the Alkyonides Gulf of the eastern Corinth rift. This part of the rift is experiencing the lowest current rates of extension; the increased level of faulting may be a function of the probable longer sedimentary record captured here. Although normal faulting dominates the core-scale deformation, the presence of a wider range of structures hints at a more complex stress field in the past. Quantification of the core structures and comparison with the seismic-scale structures imaged throughout the extensive seismic reflection network will contribute toward characterizing the extent of subseismic strain in an active rift environment. This is an elusive parameter of significance for calculating a reliable estimate of strain and estimating the integrity of petroleum reservoirs and traps.

Rift evolution

Much of the analysis to address the Expedition 381 objectives on rift evolution will result from postexpedition research. Postexpedition analyses will build on the shipboard analyses to build a high-resolution chronology for the synrift sequence sampled (e.g., biostratigraphy, tephrochronology, magnetostratigraphy, magnetic RPI, radiocarbon, and stable and radiogenic isotopes). CLSI will enable correlation of the drill cores with the extensive seismic data set, in particular increasing the precision of seismic reflector ties and time-depth conversion. These new data sets will be used to provide considerably improved constraints on ages of synrift seismic stratigraphic horizons, fault displacements, sediment thicknesses and volumes, and the timing of major rift events. Thus, we will be able to determine rift fault activity and slip rates in space and time, including in the very recent past for the purposes of hazard assessment, the timing and rate of development of the rift fault network, and the longer term rift evolution, including discrete rift phases and changes in rates of extension and subsidence. Analysis of the stratigraphic sequence, including sediment provenance and calculation of sediment fluxes in space and time, and its integration and correlation with the onshore elements of the rift sequence will allow for building a model of rift basin and sedimentary development. By tying these data with existing data and new data from drilling on the regional paleoclimate and the paleoenvironment of the basin, the relative roles of climate, tectonics, and sea level/water depth on sediment flux into the basin and the history of basin filling can be unraveled. The combined drilling data, seismic network, and preserved sequences onshore will provide a unique opportunity to

model the temporal and 3-D spatial tectonic and sedimentological development of a young rift basin.

Operations

Each site was evaluated by the EPSP before the expedition, including assessment of the subsurface with the aid of seismic reflection profiles for any potential hazards to drilling operations. Following this assessment, all sites were approved for drilling.

Site M0078

During Expedition 381, cores were recovered from two holes at Site M0078 (Figures F1, F5). In total, 20.27 days were spent on station, with an average core recovery for the site of 90.4%. Hole M0078A was drilled to 610.43 mbsf, and Hole M0078B was drilled to 55.85 mbsf.

In Hole M0078A, the WEP system was used to core the upper 75 m, and the Fugro Corer in push mode was used for the next 124 m, followed by the same corer in percussive mode for 25 m. The EXMCB (rotary) was used to core the final 386 m of the borehole. In Hole M0078B, the Fugro Corer in push mode was used throughout, to the base of the hole at 55.85 mbsf.

Transit to Hole M0078A

The *Fugro Synergy* prepared to sail on the evening of 22 October 2017, with the vessel departing the Port of Corinth at 1955 h for the first coring site. At 2130 h, the *Fugro Synergy* arrived at Site M0078, and a dynamic positioning (DP) model was established. A reference beacon was deployed, and a sound velocity profile (SVP) was conducted. Water depth near Site M0078 varied from 859 to 864 m.

Coring operations

Hole M0078A

At 0145 h on 23 October 2017, the seabed frame (SBF) was deployed, and the drilling crew began running pipe. However, running pipe took longer than anticipated due to rust at the joints resulting in the need for a thorough cleaning prior to deployment.

During the evening of 23 October, the first cores were recovered with the first core on deck at 2135 h. The SEADEVIL (an addition to the standard seabed template) was used to accurately spud in and collect a seabed/water interface sample. The WEP system was lowered to approximately 10 cm above the seabed and energized. The first core was 2.65 m long. The next attempt at coring was unsuccessful, and the decision was made to wash through this interval. Following this, coring continued throughout 23 and 24 October, generally with high recovery rates. On 25 October, recovery gradually decreased, prompting a switch to the Fugro Corer in push mode with flapper and finger catchers to optimize recovery. Initially, 3 m runs were conducted, but runs were extended to 4.7 m on the evening of 25 October.

At 2130 h, a communication issue arose with the SEADEVIL, leading to its recovery on deck at 0300 h on 26 October for assessment. Further investigation identified a printed circuit board fault, and the board was replaced. At 1415 h, the SEADEVIL was redeployed to the seabed, and the drill pipe was extended to the base of the hole so that coring could recommence. The first core was recovered on deck at 1610 h. Coring paused briefly on 26 October to undertake an in situ temperature cone penetration test (CPT) measurement at 100 mbsf; temperature CPT measurements were also taken close to 200 and 300 mbsf in Hole M0078A. Coring with

the Fugro Corer continued for the remainder of 26 October through 28 October. At 0810 h, core Run 60 made no advance, and the run was repeated at the same interval (core Run 61). A 2 m advance was achieved, but no core was returned. Next, a 4.5 m run (core Run 62) was conducted with good recovery.

Recovery became more variable on 28 and 29 October, and some runs returned no core. As a result, in the early hours of 29 October it was decided to change to using the Fugro Corer in percussive mode. Despite this change, recovery continued to be highly variable, and at 2130 h, the operational decision was made to change from the Fugro Corer to the FXMCB system.

Coring continued with good rates of advance and recovery for the next 3 days until a communications and power issue arose with the SEADEVIL, resulting in its recovery on deck at 0530 h on 2 November for further assessment. It was concluded that this issue required a significant amount of time to resolve; therefore, it was agreed that coring would continue without the use of the SEADEVIL. From this point onward, the basic SBF was used for coring without the additional support of the SEADEVIL. Coring began again at 1645 h and progressed well to 7 November.

On 7 November, coring operations were paused due to a slip clamp becoming jammed around the drill string. The clamp was eventually released after approximately 7 h. Coring then recommenced and continued through 8 November (apart from 1 h of downtime for lightning).

On the morning of 9 November, drill floor maintenance was required to repair some disk springs on the FXMCB. At ~0545 h, a slip clamp jammed around the drill string again and was not released until 0710 h, after which coring resumed. Coring paused again at 1135 h when the FXMCB was recovered on deck to undergo repairs. At 1600 h, coring resumed and progressed well through the morning of 10 November. At 1335 h, the final core from Hole M0078A was on deck with a total penetration of 610.43 mbsf.

Throughout coring operations in Hole M0078A, seawater was used as the drilling medium, with the exception of four core runs where bentonite drilling mud was used to assist with hole conditioning (removal of cuttings and reducing any swelling of the borehole sidewall).

Downhole logging operations in Hole M0078A commenced following coring and continued through 12 November. See [Logging operations](#) below for details.

Hole M0078B

Following unsuccessful logging, the decision was made to bump over by 20 m to drill a short “B” hole to capture intervals of the upper 50 m of stratigraphy that were not recovered from Hole M0078A. Pipe was tripped, and the vessel moved 20 m south to the new coordinates (38°8′41.144″N, 22°45′30.242″E).

At midnight on 12 November 2017, the *Fugro Synergy* was settling on site. The first core was recovered at 0200 h using the Fugro Corer in push mode (a 1.31 m core capturing the seabed/water interface), and coring continued throughout the day with good recovery until 1640 h, when coring operations ended at 55.85 mbsf. Seawater was used as the drilling medium throughout coring operations in Hole M0078B. Following the completion of coring, tripping pipe commenced, and the SBF was recovered on deck in preparation for transit to the port call. At 0400 h on 13 November, the *Fugro Synergy* departed Site M0078 for the pilot station and was alongside and tied up by 0630 h at the Port of Corinth.

Logging operations

The following wireline logging tools were planned for deployment in two depth stages: magnetic susceptibility and conductivity (EM51), dual laterolog resistivity (DLL3), stacked natural gamma ray (QL40SGR), sonic (QL40FWS), acoustic borehole televiewer (QL40ABI), and spectral gamma ray (ASGR512).

Hole M0078A

Following completion of coring in Hole M0078A on 10 November 2017, preparations were made for downhole logging. Hole M0078A was stabilized with weighted bentonite mud, and then the drill pipe was raised to 296.54 mbsf for the first phase of logging.

Logging with the magnetic susceptibility and conductivity (EM51) tool began at 0028 h on 11 November. The logging tools utilized for this expedition are super-slimline, and the tool strings are consequently relatively light. The light tool strings, coupled with the density of the mud that was ultimately used to stabilize the borehole, made it difficult for the tool string to descend in the borehole. Due to concerns surrounding hole stability, it was necessary to circulate heavier mud (8.5 lb/gal), which further impeded the descent of the tool string. After several failed attempts to deploy the tool, additional weight (~15 kg) was clamped to the wireline cable above the tool to make it heavier. The weighted tool started its descent more easily than before, but several losses of tension were observed, including at 297 m WSE, the depth of the drill bit, and between 337 and 347 m WSE. The total depth reached by the tool was 607 m WSE, and logging up commenced at a speed of 22 m/min. The difficulties encountered during the descent, including repeated attempts to pass various tight spots, led to the logging cable becoming entangled around the tool. As a result, 100 m of logging cable had to be cut from the primary winch (GV550). Data acquired during this first run are not depth accurate, and owing to the nature of the measurement, the recorded signal is likely unreliable due to the cable entangled around the tool. Therefore, these data have not been processed.

To save operational time, the backup winch (RG2200) was set up and used for the remainder of logging operations in Hole M0078A. To address the issues encountered during the first run, a heavier, centralized stacked tool string including the stacked natural gamma ray (QL40SGR), sonic (QL40FWS), and acoustic borehole televiewer (QL40ABI) tools was deployed. No difficulties were encountered during the descent in the drill pipe. However, the tool string could not pass through the bit into the open hole, presumably because of the passive bowspring centralizers. The tool string was recovered, and a longer, heavier tool string was deployed in its place without the bowspring centralizers and with the QL40SGR, QL40FWS, caliper (QL40CAL), and magnetic susceptibility (QL40MSUS) tools. This tool string successfully reached 607 m WSE, and logging up started at 4 m/min. Unfortunately, the tool string became stuck in the open hole (356 m WSE) during its ascent. For 6 h, multiple attempts were made to free the tool string from the borehole, with increasing load applied to the cable in a step-wise fashion. Ultimately, it became clear that recovery of the tool string might not be possible, and the breaking load of the tool head was exceeded, resulting in the abandonment of the tool string in the hole. Fishing operations were not attempted, and logging operations in Hole M0078A were concluded at 1910 h on 11 November.

Data recorded during the final run indicate that the tool string became stuck on multiple occasions during its ascent, suggesting

that borehole conditions were likely deteriorating as logging operations progressed. Owing to the difficulties encountered, data are not depth accurate, and the data quality is extremely poor.

Hole M0078B

Due to the shallow penetration (55.85 mbsf) of Hole M0078B, it was not logged.

Port call and transit to Hole M0079A

On 13 November 2017 at 0630 h, the *Fugro Synergy* made a port call in the Port of Corinth to load equipment and supplies and for an ESO and Fugro crew change. At 2020 h, the vessel departed the Port of Corinth for Site M0079. At 2223 h, the vessel arrived on site and began settling on DP. At 0210 h on 14 November, a reference beacon was deployed, and an SVP was conducted to ascertain water depth at the site.

Site M0079

Upon arrival at Site M0079, a water depth of 857.1 m was established following an SVP. In total, 18 days were spent on station, with an average core recovery of 86.65%. Drilling and coring in Hole M0079A was completed to 704.9 mbsf using two tools in 14 days. The Fugro Corer in push mode collected the upper 67 m of sediment, and the Fugro Corer in percussive mode collected the next 81 m. The FXMCB was then used to complete the lowermost 556 m of the borehole. Logging operations in Hole M0079A were conducted over 3 days.

Coring operations

Lowering the SBF began at 0240 h on 14 November 2017 and was completed by 0410 h. However, at 0515 h communications were lost to the SBF, which resulted in recovering it on deck for maintenance. At 0718 h, the bottom-hole assembly was recovered on deck, and the SBF was inspected in the moonpool then returned to the seafloor. At 1709 h on 14 November, coring commenced in Hole M0079A with the Fugro Corer in push mode. A seabed/water interface sample was collected by holding the Fugro Corer above the mudline, and 1 m of penetration was achieved, collecting 0.9 m of sediment.

Coring continued throughout the morning of 15 November until the Fugro Corer became stuck during a core run at 1045 h. Unsuccessful fishing attempts were made, therefore requiring tripping the pipe to recover the tool at 2209 h. Running pipe in the hole began at 0435 h on 16 November, and coring resumed at 1259 h. At 2223 h, there was a brief pause in coring to undertake an in situ temperature CPT measurement at 100 mbsf.

Coring continued through 17 November using the Fugro Corer alternating between percussive and push mode. On the evening of 17 November, the operational decision was made to switch to the rotary coring method (FXMCB) because recovery had dropped due to the ground conditions becoming firmer. From 18 to 23 November, coring progressed well with short pauses for high winds and three further temperature CPT measurements every ~100 m to ~400 mbsf.

At 0305 h on 24 November, repairs to the core barrel head were required, and coring resumed at 0700 h. As with Hole M0078A, it was found that penetrating to the full 5 m of the FXMCB barrel and recovering high percentages of samples was difficult at times. It appears there may have been insufficient flush at the bit to lubricate material being cored. Combined with the expanding nature of some

of the intervals, this insufficient flush apparently caused the core to compress the liner, pushing it up the core barrel and creating a gap at the bottom that allowed a section of core to expand into the gap, making it too large to enter the liner. This effectively blocked the liner, causing the remaining material to not be taken or a shorter core run to be completed. Coring progressed well until the terminal depth of the hole (704.9 mbsf) was achieved at 0045 h on 29 November.

Generally, seawater was used as the drilling medium, with the occasional use of bentonite drilling mud to assist with hole conditioning (removal of cuttings and reducing any swelling of the borehole sidewall), although bentonite was used for short runs earlier in Hole M0079A.

Logging operations

In preparation for logging, Hole M0079A was stabilized via displacement with weighted bentonite mud (8.9 lb/gal). Following the loss of a tool string in Hole M0078A, only standalone tools were available and used, and they were systematically run with a sinker bar fitted above the tool to help its descent. The planned logging program for Hole M0079A was to start logging the entire borehole through pipe with the spectral gamma ray (ASGR512) tool and then log in the open hole in three depth stages (475–705 [base of the hole], 220–475, and 50–195 mbsf) using the following tools: magnetic susceptibility and conductivity (EM51), sonic (2PSA-1000), and dual induction (DIL45). Depths of the stages changed during logging operations.

Hole M0079A logging operations started on 29 November 2017 at 0345 h, with the drill bit at 699.5 m drilling depth below seafloor (DSF) (close to the bottom of the hole) to log with the spectral gamma ray (ASGR512) tool through the pipe. The ASGR512 tool did not encounter any difficulty going down through the bentonite mud and in the pipe; it passed the drill bit to reach the bottom of the hole, and logging up started. After recovery of the tool, the drill bit was pulled up to 500 m DSF to start logging in the open hole for the first depth stage (500–705 m DSF). Bentonite mud (9 lb/gal) was circulated to stabilize the hole. Multiple attempts were made to send the magnetic susceptibility and conductivity (EM51) tool down the hole, but the tension meter of the winch (GV550) appeared to be damaged. The fault could not be identified, so it was decided to use the backup winch (RG2200) and to move to the second depth stage (220–500 m DSF). Bentonite mud was recirculated, and the drill bit was pulled up to 220 m DSF. The EM51 tool was deployed successfully and passed the drill bit, but a loss of tension was observed at 297 m WSF. After multiple attempts to pass this obstruction, it was decided to start logging up from this depth and to move to the next depth stage (50–220 m DSF). The EM51 tool was recovered, the drill bit was pulled up to 50 m DSF, and bentonite mud (9 lb/gal) was circulated. The EM51 tool was deployed without any problem and reached 230 m WSF to allow ~10 m of overlap with the data collected during the previous stage. Logging up started, the tool was recovered, and the sonic (2PSA-1000) tool was sent for the second run in this depth interval. The tool reached 230 m WSF, and no attempts were made to go deeper because the tool is fragile and deeper borehole conditions were not known. Data acquisition uphole was done and then the tool was recovered on deck. Following this run, the dual laterolog resistivity (DLL3) tool was sent instead of the dual induction (DIL45) tool because communication problems were observed with the latter during preparations on deck. The DLL3 tool was deployed successfully and

reached 290 m WSE, just above the obstruction encountered during the second depth stage. Data acquisition uphole started, and the tool was recovered safely to terminate logging operations at Site M0079, with rigging down completed at 1740 h on 1 December.

After logging operations were completed, pulling pipe and recovering the SBF and DP transponder was completed by 2325 h on 1 December. At 2340 h, transit to Site M0080 began.

Transit to Site M0080

Transit to Site M0080 began in the early hours of 2 December 2017. While in transit, four surface seawater samples were collected.

Site M0080

Drilling and coring in Hole M0080A was completed to 534.1 mbsf in 13 days, achieving an 84% recovery rate. The Fugro Corer in both push and percussive modes collected the upper 141 m of sediment. The FXMCB was used to complete the lower 390 m of the borehole. Wireline logging operations were then conducted over 2 days.

Coring operations

During the positioning process for Hole M0080A on 2 December 2017, the SBF and pipe were lowered to within 50 m of the seafloor. After positioning was complete, the SBF and pipe were lowered, and coring commenced using the Fugro Corer in push mode. A seabed/water interface sample was collected. The corer was dropped through the drill string in free fall and penetrated 1.5 m with a recovery of 1.4 m of sediment. Coring continued uninterrupted for the rest of 2 December and throughout 3 December, with exceptional progress being made at a rate of >100 m/day. A switch to the Fugro Corer percussive mode occurred at 84 mbsf. The ability to alternate between push and percussive modes without switching to the rotary method (FXMCB) enabled nonrotary coring to greater depths than would have otherwise been possible. A temperature CPT measurement was made at close to 100 mbsf to acquire in situ temperature and friction/strength information of the formation, and a second temperature CPT measurement was taken close to 210 mbsf. The change to the FXMCB was made on the evening of 3 December when the efficacy of the Fugro Corer had dropped and the sediments were deemed firm enough to withstand the effects of rotary coring. Following the switch to the FXMCB, coring continued at a very high rate until the morning of 5 December. At that time, the ground conditions became considerably more challenging, with mixed beds of sands and gravels, resulting in a slowing of the rate of advance to 29.6 m/day. These slow rates continued and worsened until the end of 12 December, with the lowest advance of 20.0 m/day in Hole M0080A on 9 December. Coring continued uninterrupted during this period.

The rate of advance improved significantly throughout 12 and 13 December, with 85.4 m of advance, due to favorable ground conditions. The drilling rate slowed once more on 14 December as conditions became more challenging.

The final core from Hole M0080A was recovered at 0330 h on 15 December, achieving a final depth of 534.1 mbsf. Despite a small number of discrete areas where recovery was low, Hole M0080A achieved good recovery (84%). The borehole was cored 65 m deeper than anticipated because the scientific goal for this borehole (basement) was deeper than the initial estimated target depth. Basement *sensu stricto* was not reached; however, the deepest cores recovered very coarse grained conglomerates thought to immediately overlie basement.

In general, seawater was used as the drilling medium; however, bentonite was used for core Runs 64–103 and 127–146.

Logging operations

In preparation for logging, Hole M0080A was stabilized via displacement with weighted bentonite mud (8.8 lb/gal). Standalone tools were used to address the scientific objectives, and they were systematically run with a sinker bar fitted above each tool to help its descent. Logging the hole started through the pipe with the spectral gamma ray (ASGR512) tool and then continued in three depth stages where the following tools were planned to be deployed in the open hole: magnetic susceptibility and conductivity (EM51), sonic (2PSA-1000), dual induction (DIL45), and ASGR512.

All tools were run with the primary winch (GV550). Hole M0080A logging started on 15 December 2017 at 0330 h with the drill bit pulled up to 533.1 m DSF (just above the base of the hole) to log through the pipe. The spectral gamma ray (ASGR512) tool did not encounter any difficulty going down through the bentonite mud and in the pipe; it passed the drill bit to reach the bottom of the hole, and logging up started. After recovery of the ASGR512 tool, the drill bit was pulled up to 365 m DSF to log in the open hole for the first depth stage (365–533 m DSF). Bentonite mud (8.8 lb/gal) was circulated to stabilize the hole. The magnetic susceptibility and conductivity (EM51) tool was deployed and passed the drill bit, but difficulties were encountered in the open hole from 410 to 425 m WSE, with several losses of tension. After borehole conditions prevented the tool from passing beyond 425 m WSE, data were collected from this depth to the drill bit and the tool was recovered on deck to perform a wiper trip downhole. The drill string was lowered to the bottom of the hole and then pulled up to 430 m WSE to avoid the interval where losses of tension were observed during the previous run. The EM51 and sonic (2PSA-1000) tools were run successfully, reaching a maximum depth of ~530 m WSE and collecting data from this depth to the drill bit at 430 m WSE. However, when deploying the ASGR512 tool, the tool could not continue its descent beyond ~10 m below the drill bit. The decision was made to move to the next depth stage, and the drill bit was lowered to 460 m DSF to clean the borehole walls and then pulled to 230 m DSF for the second depth stage. In this depth interval, the EM51 tool was run down the hole but could not pass beyond ~430 m WSE. Data were collected with the EM51 tool from 430 to 230 m WSE. The 2PSA-1000 tool was deployed but could not pass beyond ~370 m WSE; therefore, data were collected up from this depth to the drill bit at 230 m DSF. After recovery of the 2PSA-1000 tool, the dual induction (DIL45) tool and then the ASGR512 tool were deployed successfully in a similar depth range, collecting data from 370 to 230 m WSE. The third and last depth stage was conducted after the drill bit had been pulled up to 50 m DSF, and the bentonite present in the borehole was displaced with seawater. This change in fluid was aimed at better stabilizing the borehole for the expected lithologies in this shallow interval. Once deployed, the first tool (EM51) could not pass beyond ~220 m WSE downhole. The EM51, 2PSA-1000, DIL45, and ASGR512 tools were all deployed with data acquisition from ~220 to 50 m WSE. Logging operations were completed at 1235 h on 17 December.

Demobilization

Following the completion of logging operations in Hole M0080A, the ESO team continued with demobilizing the containerized laboratories and offices. All operations ceased at 1235 h on 17 December 2017, and the *Fugro Synergy* drill team tripped out of the

hole. Transit to Corinth took place overnight, with the *Fugro Synergy* arriving dockside at 0600 h on 18 December.

Outreach and communication

The overall aim of the ESO Outreach and Education effort is to promote the benefits of each expedition's science and the wider objectives of IODP/ECORD to a broad audience, including the science community and public. To accomplish this objective, we focused on publicizing the expedition's aims and findings to international media and concentrated on media networks developed in the IODP/ECORD community and members of the science party's organizations.

Targeted activities in support of the outreach and communication objectives included the following:

- The expedition web page on the ECORD website, which acts as a source of information by including Ship Reports and blogs, includes links to expedition materials and a media pack with information about press conferences and media releases along with pictures and contact details to arrange interviews with the expedition scientists.
- Expedition promotional materials, including an expedition logo, flier (in English), and branded items such as caps, T-shirts, iron on patches, and mugs were available for the science party members, ESO staff, and ship's crew.
- Banners with IODP and ECORD logos and the expedition logo were available to display on the side of the *Fugro Synergy* and serve as a backdrop for interviews and pictures. Widespread use of logos ensures recognition in photographs/videos.
- Contact was made with media officers at the science party member's universities to raise awareness of their staff's participation in the expedition and to enlist their support in promoting the expedition locally and nationally.
- A media day was held at the start of the expedition on 19 October 2017 at the Alexandreio Conference Centre in Loutraki, Greece. Professor Lisa McNeill, Professor Donna Shillington (Co-Chief Scientists), and Gareth Carter (ESO, Expedition Project Manager) presented logistics and expedition objectives. Afterward, a visit on board the *Fugro Synergy* took place. The event was attended by a TV team from Athens (Skai TV) and by Greek scientist collaborators on the project. After the media day, a local TV team visited the vessel (Hlektra TV). Prior to the expedition, there was a news feature in one of the main German language newspapers in Europe.
- For the on board media day, an embargoed press release was issued to IODP/ECORD representatives, media departments of the participants, Greek media, and international media. Over 20 news articles covered the project, particularly in the Corinth region of Greece.
- Education officer Martin Böttcher (education officer and teacher) visited the *Fugro Synergy* at the Port in Corinth before the offshore phase of expedition and then visited the University of Bremen during the OSP. He hosted a ship-to-shore event with the Rabanus-Maurus-Schule in Fulda, Germany, and wrote two blog stories about the expedition.
- Several ship-to-shore events were broadcast, including to staff and students at the University of Athens, hosted locally by science party member Katerina Kouli, and to the science party of the R/V *JOIDES Resolution* in transit to New Zealand during IODP Expedition 372.
- A video tour and scientific presentation was recorded for the UK Natural Environment Research Council Showcase "Unearthed" Exhibition at Our Dynamic Earth (Edinburgh UK). This event was visited by over 7000 members of the public.
- Video footage was recorded about life and scientific objectives on board the research vessel, including short interviews, core flow offshore, and aerial video of the *Fugro Synergy* recorded by UAV drone. All clips are published on the ECORD/ESO YouTube channel (<http://www.youtube.com/user/ECORDESO>).
- A second media event was held during the OSP on 22 February 2018 at MARUM and featured short presentations by the Co-Chief Scientists followed by interviews and a tour of the laboratory facilities and core repository. The event was attended by representatives from regional and national media and reported nationally in printed and online media.
- A second press release was issued on 5 March, which was picked up by universities and institutions that published individual versions that resulted in features by various international media.
- Regular promotion of the expedition's accomplishments onshore and offshore were posted on ECORD's social media platforms such as Twitter, Facebook (summary statistics unavailable), and YouTube (2000 views plus reposts to Facebook and Twitter).
- An expedition blog (<https://esoexp381corinthactiveriftdevelopment.wordpress.com>) was maintained throughout the expedition (onshore and offshore) and included regular updates from all phases of the expedition. Between the start of the offshore phase and the end of the OSP, the blog site had been visited over 21,200 times.
- During the OSP in Bremen, short video clips of the core flow were produced, as well as audio recordings and pictures to be published in due course. They supplement the series of offshore videos that have already been uploaded on the ECORD/ESO YouTube channel.

References

- Andrews, J.E., Portman, C., Rowe, P.J., Leeder, M.R., and Kramers, J.D., 2007. Sub-orbital sea-level change in early MIS 5e: new evidence from the Gulf of Corinth, Greece. *Earth and Planetary Science Letters*, 259(3–4):457–468. <https://doi.org/10.1016/j.epsl.2007.05.005>
- Anthonissen, D.E., and Ogg, J.G., 2012. Appendix 3—Cenozoic and Cretaceous biochronology of planktonic foraminifera and calcareous nannofossils. In Gradstein, F.M., Ogg, J.G., Schmitz, M.D., and Ogg, G.M., (Eds.), *The Geologic Time Scale 2012*: Amsterdam (Elsevier), 1083–1127. <https://doi.org/10.1016/B978-0-444-59425-9.15003-6>
- Armijo, R., Meyer, B., King, G.C.P., Rigo, A., and Papanastassiou, D., 1996. Quaternary evolution of the Corinth rift and its implications for the Late Cenozoic evolution of the Aegean. *Geophysical Journal International*, 126(1):11–53. <https://doi.org/10.1111/j.1365-246X.1996.tb05264.x>
- Avallone, A., Briole, P., Agatza-Balodimou, A.M., Billiris, H., Charade, O., Mitsakaki, C., Necessian, A., Papazissi, K., Paradissis, D., and Veis, G., 2004. Analysis of eleven years of deformation measured by GPS in the Corinth Rift Laboratory area. *Comptes Rendus Geosciences*, 336(4–5):301–311. <https://doi.org/10.1016/j.crte.2003.12.007>
- Backert, N., Ford, M., and Malartre, F., 2010. Architecture and sedimentology of the Kerinitis Gilbert-type fan delta, Corinth rift, Greece. *Sedimentology*, 57(2):543–586. <https://doi.org/10.1111/j.1365-3091.2009.01105.x>
- Bayrakci, G., Minshull, T.A., Sawyer, D.S., Reston, T.J., Klaeschen, D., Papenberg, C., Ranero, C., et al., 2016. Fault-controlled hydration of the upper mantle during continental rifting. *Nature Geoscience*, 9(5):384–388. <https://doi.org/10.1038/ngeo2671>

- Bell, R.E., McNeill, L.C., Bull, J.M., and Henstock, T.J., 2008. Evolution of the offshore western Gulf of Corinth. *Geological Society of America Bulletin*, 120(1–2):156–178. <https://doi.org/10.1130/B26212.1>
- Bell, R.E., McNeill, L.C., Bull, J.M., Henstock, T.J., Collier, R.E.L., and Leeder, M.R., 2009. Fault architecture, basin structure and evolution of the Gulf of Corinth rift, central Greece. *Basin Research*, 21(6):824–855. <https://doi.org/10.1111/j.1365-2117.2009.00401.x>
- Bell, R.E., McNeill, L.C., Henstock, T.J., and Bull, J.M., 2011. Comparing extension on multiple time and depth scales in the Corinth rift, central Greece. *Geophysical Journal International*, 186(2):463–470. <https://doi.org/10.1111/j.1365-246X.2011.05077.x>
- Bentham, P., Collier, R.E., Gawthorpe, R.L., Leeder, R., and Stark, C., 1991. Tectono-sedimentary development of an extensional basin: the Neogene Megara Basin, Greece. *Journal of the Geological Society*, 148(5):923–934. <https://doi.org/10.1144/gsjgs.148.5.0923>
- Bernard, P., Lyon-Caen, H., Briole, P., Deschamps, A., Boudin, F., Makropoulos, K., Papadimitriou, P., Lemeille, F., Patau, G., Billiris, H., Paradissis, D., Papazissi, K., Castarède, H., Charade, O., Nercessian, A., Avallone, A., Pacchiani, F., Zahradnik, J., Sacks, S., and Linde, A., 2006. Seismicity, deformation and seismic hazard in the western rift of Corinth: new insights from the Corinth Rift Laboratory (CRL). *Tectonophysics*, 426(1–2):7–30. <https://doi.org/10.1016/j.tecto.2006.02.012>
- Bialas, R.W., and Buck, W.R., 2009. How sediment promotes narrow rifting: application to the Gulf of California. *Tectonics*, 28(4):TC4014. <https://doi.org/10.1029/2008TC002394>
- Briole, P., Rigo, A., Lyon-Caen, H., Ruegg, J.C., Papazissi, K., Mitsakaki, C., Balodimou, A., Veis, G., Hatzfeld, D., and Deschamps, A., 2000. Active deformation of the Corinth rift, Greece: results from repeated global positioning system surveys between 1990 and 1995. *Journal of Geophysical Research: Solid Earth*, 105(B11):25605–25625. <https://doi.org/10.1029/2000JB900148>
- Burov, E., and Poliakov, A., 2001. Erosion and rheology controls on synrift and postrift evolution: verifying old and new ideas using a fully coupled numerical model. *Journal of Geophysical Research: Solid Earth*, 106(B8):16461–16481. <https://doi.org/10.1029/2001JB000433>
- Channell, J.E.T., Hodell, D.A., Xuan, C., Mazaud, A., and Stoner, J.S., 2008. Age calibrated relative paleointensity for the last 1.5 Myr at IODP Site U1308 (North Atlantic). *Earth and Planetary Science Letters*, 274(1–2):59–71. <https://doi.org/10.1016/j.epsl.2008.07.005>
- Channell, J.E.T., Xuan, C., and Hodell, D.A., 2009. Stacking paleointensity and oxygen isotope data for the last 1.5 Myr (PISO-1500). *Earth and Planetary Science Letters*, 283(1–4):14–23. <https://doi.org/10.1016/j.epsl.2009.03.012>
- Charalampakis, M., Lykousis, V., Sakellariou, D., Papatheodorou, G., and Ferentinos, G., 2014. The tectono-sedimentary evolution of the Lechaion Gulf, the south eastern branch of the Corinth graben, Greece. *Marine Geology*, 351:58–75. <https://doi.org/10.1016/j.margeo.2014.03.014>
- Clarke, P.J., Davies, R.R., England, P.C., Parson, B., Billiris, H., Paradissis, D., Veis, G., Cross, P.A., Denys, P.H., Ashkenazi, V., Bingley, R., Kahle, H.-G., Muller, M.-V., and Briole, P., 1998. Crustal strain in central Greece from repeated GPS measurements in the interval 1989–1997. *Geophysical Journal International*, 135(1):195–214. <https://doi.org/10.1046/j.1365-246X.1998.00633.x>
- Collier, R.E.L., Leeder, M.R., Trout, M., Ferentinos, G., Lyberis, E., and Papatheodorou, G., 2000. High sediment yields and cool, wet winters: test of last glacial paleoclimates in the northern Mediterranean. *Geology*, 28(11):999–1002. [https://doi.org/10.1130/0091-7613\(2000\)28<999:HSYACW>2.0.CO;2](https://doi.org/10.1130/0091-7613(2000)28<999:HSYACW>2.0.CO;2)
- Ford, M., Hemelsdaël, R., Mancini, M., and Palyvos, N., 2016. Rift migration and lateral propagation: evolution of normal faults and sediment-routing systems of the western Corinth rift (Greece). In Childs, C., Holdsworth, R.E., Jackson, C.A.-L., Manzocchi, T., Walsh, J.J., and Yielding, G. (Eds.), *The Geometry and Growth of Normal Faults*. Geological Society Special Publication, 439:131–168. <https://doi.org/10.1144/SP439.15>
- Ford, M., Rohais, S., Williams, E.A., Bourlange, S., Jousselin, D., Backert, N., and Malartre, F., 2013. Tectono-sedimentary evolution of the western Corinth rift (central Greece). *Basin Research*, 25(1):3–25. <https://doi.org/10.1111/j.1365-2117.2012.00550.x>
- Ford, M., Williams, E.A., Malartre, F., and Popescu, S.-M., 2007. Stratigraphic architecture, sedimentology and structure of the Vouraikos Gilbert-type fan delta, Gulf of Corinth, Greece. In Nichols, G., Paola, C., and Williams, E. (Eds.), *Sedimentary Processes, Environments and Basins: A Tribute to Peter Friend*. Jarvis, I. (Series Ed.). Special Publication of the International Association of Sedimentologists, 38:44–90. <https://doi.org/10.1002/9781444304411.ch4>
- Gawthorpe, R.L., Jackson, C.A.-L., Young, M.J., Sharp, I.R., Moustafa, A.R., and Leppard, C.W., 2003. Normal fault growth, displacement localisation and the evolution of normal fault populations: the Hammam Faraun fault block, Suez rift, Egypt. *Journal of Structural Geology*, 25(6):883–895. [https://doi.org/10.1016/S0191-8141\(02\)00088-3](https://doi.org/10.1016/S0191-8141(02)00088-3)
- Gawthorpe, R.L., and Leeder, M.R., 2000. Tectono-sedimentary evolution of active extensional basins. *Basin Research*, 12(3–4):195–218. <https://doi.org/10.1111/j.1365-2117.2000.00121.x>
- Gawthorpe, R.L., Leeder, M.R., Haralambos, K., Skourtsos, E., Andrews, J.E., Henstra, G.A., Mack, G.H., Muravchik, M., Turner, J.A., and Stamatakis, M., 2017. Tectono-sedimentary evolution of the Plio–Pleistocene Corinth rift, Greece. *Basin Research*. <https://doi.org/10.1111/bre.12260>
- Hemelsdaël, R., Ford, M., Malartre, F., and Gawthorpe, R., 2017. Interaction of an antecedent fluvial system with early normal fault growth: implications for syn-rift stratigraphy, western Corinth rift (Greece). *Sedimentology*, 64(7):1957–1997. <https://doi.org/10.1111/sed.12381>
- Higgs, B., 1988. Syn-sedimentary structural controls on basin deformation in the Gulf of Corinth, Greece. *Basin Research*, 1(3):155–165. <https://doi.org/10.1111/j.1365-2117.1988.tb00012.x>
- Huismans, R.S., and Beaumont, C., 2007. Roles of lithospheric strain softening and heterogeneity in determining the geometry of rifts and continental margins. *Geological Society Special Publications*, 282(1):111–138. <https://doi.org/10.1144/SP282.6>
- Huismans, R., and Beaumont, C., 2011. Depth-dependent extension, two-stage breakup and cratonic underplating at rifted margins. *Nature*, 473(7345):74–78. <https://doi.org/10.1038/nature09988>
- Jolivet, L., 2001. A comparison of geodetic and finite strain pattern in the Aegean, geodynamic implications. *Earth and Planetary Science Letters*, 187(1–2):95–104. [https://doi.org/10.1016/S0012-821X\(01\)00277-1](https://doi.org/10.1016/S0012-821X(01)00277-1)
- Jolivet, L., Brun, J.-P., Gautier, P., Lallament, S., and Patria, M., 1994. 3D-kinematics of extension in the Aegean region from the early Miocene to the present: insights from the ductile crust. *Bulletin de la Société Géologique de France*, 165(3):195–209. <http://bsgf.geoscienceworld.org/content/gssgfbull/165/3/195.full.pdf>
- Jolivet, L., Labrousse, L., Agard, P., Lacombe, O., Bailly, V., Lecomte, E., Mouthereau, F., and Mehl, C., 2010. Rifting and shallow-dipping detachments, clues from the Corinth rift and the Aegean. *Tectonophysics*, 483(3–4):287–304. <https://doi.org/10.1016/j.tecto.2009.11.001>
- Lavier, L.L., and Buck, W.R., 2002. Half graben versus large-offset low-angle normal fault: importance of keeping cool during normal faulting. *Journal of Geophysical Research: Solid Earth*, 107(B6):ETG 8-1–ETG 8-13. <https://doi.org/10.1029/2001JB000513>
- Lavier, L.L., and Manatschal, G., 2006. A mechanism to thin the continental lithosphere at magma-poor margins. *Nature*, 440(7082):324–328. <https://doi.org/10.1038/nature04608>
- Le Pichon, X., and Angelier, J., 1981. Extensional tectonics associated with convergent plate boundaries —the Aegean Sea. *Philosophical Transactions of the Royal Society, A: Mathematical, Physical & Engineering Sciences*, 300(1454):357–372. <https://doi.org/10.1098/rsta.1981.0069>
- Leeder, M.R., Collier, R.E.L., Abdul Aziz, L.H., Trout, M., Ferentinos, G., Papatheodorou, G., and Lyberis, E., 2002. Tectono-sedimentary processes along an active marine/lacustrine half-graben margin: Alkyonides Gulf, E. Gulf of Corinth, Greece. *Basin Research*, 14(1):25–41. <https://doi.org/10.1046/j.1365-2117.2002.00164.x>
- Leeder, M.R., Mack, G.H., Brasier, A.T., Parrish, R.R., McIntosh, W.C., Andrews, J.E., and Duermeijer, C.E., 2008. Late-Pliocene timing of Corinth (Greece) rift-margin fault migration. *Earth and Planetary Science Letters*, 274(1–2):132–141. <https://doi.org/10.1016/j.epsl.2008.07.006>

- Leeder, M.R., Mark, D.F., Gawthorpe, R.L., Kranis, H., Loveless, S., Peden-tchouk, N., Skourtsos, E., Turner, J., Andrews, J.E., and Stamatakis, M., 2012. A “Great Deepening”: chronology of rift climax, Corinth rift, Greece. *Geology*, 40(11):999–1002. <https://doi.org/10.1130/G33360.1>
- Leeder, M.R., Portman, C., Andrews, J.E., Collier, R.E.L., Finch, E., Gawthorpe, R.L., McNeill, L.C., Pérez-Arluca, M., and Rowe, P., 2005. Normal faulting and crustal deformation, Alkyonides Gulf and Perachora Peninsula, eastern Gulf of Corinth rift, Greece. *Journal of the Geological Society*, 162(3):549–561. <https://doi.org/10.1144/0016-764904-075>
- Lund, S.P., Schwartz, M., Keigwin, L., and Johnson, T., 2005. Deep-sea sediment records of the Laschamp geomagnetic field excursion (~41,000 calendar years before present). *Journal of Geophysical Research: Solid Earth*, 110(B4):B04101. <https://doi.org/10.1029/2003JB002943>
- Lykousis, V., Sakellariou, D., Moretti, I., and Kaberi, H., 2007. Late Quaternary basin evolution of the Gulf of Corinth: sequence stratigraphy, sedimentation, fault-slip and subsidence rates. *Tectonophysics*, 440(1–4):29–51. <https://doi.org/10.1016/j.tecto.2006.11.007>
- Manatschal, G., Froitzheim, N., Rubenach, M., and Turrin, B., 2001. The role of detachment faulting in the formation of an ocean-continent transition: insights from the Iberia Abyssal Plain. In Wilson, R.C.L., Whitmarsh, R.B., Taylor, B., and Froitzheim, N. (Eds.), *Non-Volcanic Rifting of Continental Margins: A Comparison of Evidence from Land and Sea*. Geological Society Special Publication, 187(1):405–428. <http://dx.doi.org/10.1144/GSL.SP.2001.187.01.20>
- McHugh, C.M.G., Gurung, D., Giosan, L., Ryan, W.B.F., Mart, Y., Sancar, U., Burckle, L., and Çagatay, M.N., 2008. The last reconnection of the Marmara Sea (Turkey) to the World Ocean: a paleoceanographic and paleoclimatic perspective. *Marine Geology*, 255(1–2):64–82. <https://doi.org/10.1016/j.margeo.2008.07.005>
- McKenzie, D., 1978. Some remarks on the development of sedimentary basins. *Earth and Planetary Science Letters*, 40(1):25–32. [https://doi.org/10.1016/0012-821X\(78\)90071-7](https://doi.org/10.1016/0012-821X(78)90071-7)
- McLeod, A.E., Dawers, N.H., and Underhill, J.R., 2000. The propagation and linkage of normal faults: insights from the Strathspey-Brent-Statfjord fault array, northern North Sea. *Basin Research*, 12(3–4):263–284. <https://doi.org/10.1111/j.1365-2117.2000.00124.x>
- McNeill, L.C., Cotterill, C.J., Henstock, T.J., Bull, J.M., Stafatos, A., Collier, R.E.L., Papatheoderou, G., Ferentinos, G., and Hicks, S.E., 2005. Active faulting within the offshore western Gulf of Corinth, Greece: implications for models of continental rift deformation. *Geology*, 33(4):241–244. <https://doi.org/10.1130/G21127.1>
- Moretti, I., Lykousis, V., Sakellariou, D., Reynaud, J.-Y., Benziane, B., and Prinzhofer, A., 2004. Sedimentation and subsidence rate in the Gulf of Corinth: what we learn from the *Marion Dufresne's* long-piston coring. *Comptes Rendus Geoscience*, 336(4–5):291–299. <https://doi.org/10.1016/j.crte.2003.11.011>
- Nixon, C.W., McNeill, L.C., Bull, J.M., Bell, R.E., Gawthorpe, R.L., Henstock, T.J., Christodoulou, D., et al., 2016. Rapid spatiotemporal variations in rift structure during development of the Corinth rift, central Greece. *Tectonics*, 35(5):1225–1248. <https://doi.org/10.1002/2015TC004026>
- Olive, J.-A., Behn, M.D., and Malatesta, L.C., 2014. Modes of extensional faulting controlled by surface processes. *Geophysical Research Letters*, 41(19):6725–6733. <https://doi.org/10.1002/2014GL061507>
- Osmundsen, P.T., and Ebbing, J., 2008. Styles of extension offshore mid-Norway and implications for mechanisms of crustal thinning at passive margins. *Tectonics*, 27(6):TC6016. <https://doi.org/10.1029/2007TC002242>
- Perissoratis, C., Piper, D.J.W., and Lykousis, V., 2000. Alternating marine and lacustrine sedimentation during late Quaternary in the Gulf of Corinth rift basin, central Greece. *Marine Geology*, 167(3–4):391–411. [https://doi.org/10.1016/S0025-3227\(00\)00038-4](https://doi.org/10.1016/S0025-3227(00)00038-4)
- Rohais, S., Eschard, R., Ford, M., Guillocheau, F., and Moretti, I., 2007. Stratigraphic architecture of the Plio–Pleistocene infill of the Corinth rift: implications for its structural evolution. *Tectonophysics*, 440(1–4):5–28. <https://doi.org/10.1016/j.tecto.2006.11.006>
- Rohling, E.J., Marino, G., and Grant, K.M., 2015. Mediterranean climate and oceanography, and the periodic development of anoxic events (sapropels). *Earth-Science Reviews*, 143: 62–97. <https://doi.org/10.1016/j.earscirev.2015.01.008>
- Sachpazi, M., Clément, C., Laigle, M., Hirn, A., and Roussos, N., 2003. Rift structure, evolution, and earthquakes in the Gulf of Corinth, from reflection seismic images. *Earth and Planetary Science Letters*, 216(3):243–257. [https://doi.org/10.1016/S0012-821X\(03\)00503-X](https://doi.org/10.1016/S0012-821X(03)00503-X)
- Sachpazi, M., Galvé, A., Laigle, M., Hirn, A., Sokos, E., Serpetsidaki, A., Marthelot, J.-M., Pi Alperin, J.M., Zelt, B., and Taylor, B., 2007. Moho topography under central Greece and its compensation by Pn time-terms for the accurate location of hypocenters: the example of the Gulf of Corinth 1995 Aigion earthquake. *Tectonophysics*, 440(1–4):53–65. <https://doi.org/10.1016/j.tecto.2007.01.009>
- Sadori, L., Koutsodendris, A., Panagiotopoulos, K., Masi, A., Bertini, A., Combourieu-Nebout, N., Francke, A., et al., 2016. Pollen-based paleo-environmental and paleoclimatic change at Lake Ohrid (south-eastern Europe) during the past 500 ka. *Biogeosciences*, 13(5):1423–1437. <https://doi.org/10.5194/bg-13-1423-2016>
- Sakellariou, D., Lykousis, V., Alexandri, S., Kaberi, H., Rousakis, G., Nomikou, P., Georgiou, P., and Ballas, D., 2007. Faulting, seismic-stratigraphic architecture and Late Quaternary evolution of the Gulf of Alkyonides Basin–East Gulf of Corinth, Central Greece. *Basin Research*, 19(2):273–295. <https://doi.org/10.1111/j.1365-2117.2007.00322.x>
- Scholz, C.A., Johnson, T.C., Cohen, A.S., King, J.W., Peck, J.A., Overpeck, J.T., Talbot, M.R., et al., 2007. East African megadroughts between 135 and 75 thousand years ago and bearing on early-modern human origins. *Proceedings of the National Academy of Sciences*, 104(42):16416–16421. <https://doi.org/10.1073/pnas.0703874104>
- Sharp, I.R., Gawthorpe, R.L., Underhill, J.R., and Gupta, S., 2000. Fault-propagation folding in extensional settings: examples of structural style and synrift sedimentary response from the Suez rift, Sinai, Egypt. *Geological Society of America Bulletin*, 112(12):1877–1899. [https://doi.org/10.1130/0016-7606\(2000\)112<1877:FPFIES>2.0.CO;2](https://doi.org/10.1130/0016-7606(2000)112<1877:FPFIES>2.0.CO;2)
- Skourtsos, E., and Kranis, H., 2009. Structure and evolution of the western Corinth rift, through new field data from the northern Peloponnese. In Ring, U., and Wernicke, B. (Eds.), *Extending a Continent: Architecture, Rheology and Heat Budget*. Geological Society Special Publication, 321(1):119–138. <https://doi.org/10.1144/SP321.6>
- Stafatos, A., Papatheodorou, G., Ferentinos, G., Leeder, M., and Collier, R., 2002. Seismic reflection imaging of active offshore faults in the Gulf of Corinth, Greece: their seismotectonic significance. *Basin Research*, 14(4):487–502. <https://doi.org/10.1046/j.1365-2117.2002.00176.x>
- Stott, L., Poulsen, C., Lund, S., and Thunell, R., 2002. Super ENSO and global climate oscillations at millennial time scales. *Science*, 297(5579):222–226. <https://doi.org/10.1126/science.1071627>
- Taylor, B., Weiss, J.R., Goodliffe, A.M., Sachpazi, M., Laigle, M., and Hirn, A., 2011. The structures, stratigraphy and evolution of the Gulf of Corinth rift, Greece. *Geophysical Journal International*, 185(3):1189–1219. <https://doi.org/10.1111/j.1365-246X.2011.05014.x>
- Taylor, S.K., Bull, J.M., Lamarche, G., and Barnes, P.M., 2004. Normal fault growth and linkage in the Whakatane Graben, New Zealand, during the last 1.3 Myr. *Journal of Geophysical Research: Solid Earth*, 109(B2):B02408. <https://doi.org/10.1029/2003JB002412>
- Tiberi, C., Lyon-Caen, H., Hatzfeld, D., Achauer, U., Karagianni, E., Kiratzi, A., Louvari, E. et al., 2000. Crustal and upper mantle structure beneath the Corinth rift (Greece) from a teleseismic tomography study. *Journal of Geophysical Research: Solid Earth*, 105(B12):28159–28171. <https://doi.org/10.1029/2000JB900216>
- Tzedakis, P.C., Pälike, H., Roucoux, K.H., and de Abreu, L., 2009. Atmospheric methane, southern European vegetation and low–mid latitude links on orbital and millennial timescales. *Earth and Planetary Science Letters*, 277(3–4):307–317. <http://dx.doi.org/10.1016/j.epsl.2008.10.027>

- Valet, J.-P., Meynadier, L., and Guyodo, Y., 2005. Geomagnetic dipole strength and reversal rate over the past two million years. *Nature*, 435(7043):802–805. <https://doi.org/10.1038/nature03674>
- Van Avendonk, H.J.A., Lavier, L.L., Shillington, D.J., and Manatschal, G., 2009. Extension of continental crust at the margin of the eastern Grand Banks, Newfoundland. *Tectonophysics*, 468(1–4):131–148. <https://doi.org/10.1016/j.tecto.2008.05.030>
- Whitmarsh, R.B., Manatschal, G., and Minshull, T.A., 2001. Evolution of magma-poor continental margins from rifting to seafloor spreading. *Nature*, 413(6852):150–154. <https://doi.org/10.1038/35093085>
- Zelt, B.C., Taylor, B., Sachpazi, M., and Hirn, A., 2005. Crustal velocity and Moho structure beneath the Gulf of Corinth, Greece. *Geophysical Journal International*, 162(1):257–268. <https://doi.org/10.1111/j.1365-246X.2005.02640.x>
- Zelt, B.C., Taylor, B., Weiss, J.R., Goodliffe, A.M., Sachpazi, M., and Hirn, A., 2004. Streamer tomography velocity models for the Gulf of Corinth and Gulf of Itea, Greece. *Geophysical Journal International*, 159(1):333–346. <https://doi.org/10.1111/j.1365-246X.2004.02388.x>

Table T1. Onshore and offshore measurements, Expedition 381. BCR = Bremen Core Repository. IW = interstitial water, ICP-OES = inductively coupled plasma-optical emission spectrometry, IC = ion chromatography, TOC = total organic carbon, TC = total carbon, LECO = carbon/sulfur analyzer, XRF = X-ray fluorescence, ED-XRF = energy dispersive XRF, MSCL = multisensor core logger, XRD = X-ray diffraction, CPT = cone penetration test, OSP = Onshore Science Party.

D/V <i>Fugro Synergy</i> , offshore Corinth	Onshore science party, BCR (Germany)
Core description	Core description: split-core visual core description and smear slide analysis
Core catcher description	Micropaleontology: foraminifers, palynology, diatoms, and nannofossils
Micropaleontology: diatoms, nannofossils, and foraminifers	Geochemistry IW analysis: ICP-OES (major and trace elements) and IC (chloride, bromide, sulfate, and nitrate)
Geochemistry: pH by ion-specific electrode, alkalinity by single-point titration to pH, salinity by refractometer, ammonium by flow injection method, and sampling for postexpedition research for time-sensitive analyses	Geochemistry solid phase analysis: TOC/TC by LECO (carbon-sulfur analysis) and XRF bulk element analysis by ED-XRF
Whole-core MSCL logging: density, velocity, magnetic susceptibility, electrical resistivity, and natural gamma ray	XRD bulk mineralogy analysis
Core catcher photography	Discrete sample measurements: moisture and density properties (bulk and grain density and water content porosity), and compressional <i>P</i> -wave velocity
Downhole logging: total gamma, spectral gamma, resistivity, sonic, conductivity, and magnetic susceptibility	Core imaging
Shear strength (handheld penetrometer and downhole CPT)	Shear strength (shear vane and fall cone)
Downhole temperature (CPT)	High-resolution continuous digital line scanning of all split-core surfaces
	Thermal conductivity on whole cores (pre-OSP) and color reflectance and <i>P</i> -wave measurements on split-core surface
	Discrete paleomagnetic measurements and discrete magnetic susceptibility measurements

Table T2. Hole locations, water depths, core, and operational information, Expedition 381.

Hole	Latitude	Longitude	Water depth (mbsl)	Core runs	Interval cored (m)	Interval recovered (m)	Core recovery (%)	Interval open holed (m)	Penetration depth (mbsf)	Time on site (days)
M0078A	38°8'41.802"N	22°45'30.251"E	859.5	176	610.43	533.99	87	0	610.43	21
M0078B	38°8'41.144"N	22°45'30.242"E	864.0	15	55.85	52.17	93	0	55.85	1
M0079A	38°9'30.243"N	22°41'43.316"E	857.1	163	704.90	610.80	87	0	704.90	16
M0080A	38°7'12.147"N	23°5'10.614"E	348.8	146	534.10	447.83	84	0	534.10	16

Table T3. Definitions of facies associations used in lithostratigraphic interpretation, Expedition 381.

Facies association	Definition
FA1	Homogeneous mud
FA2	Greenish gray mud with dark gray to black mud to sand beds and laminations
FA3	Light gray to white laminations alternating with mud and silt beds
FA4	Laminated greenish gray to gray mud with mud beds
FA5	Greenish gray mud with homogeneous centimeter-thick gray mud beds
FA6	Green bedded partly bioturbated mud, silt, and sand
FA7	Clast-supported sandy conglomerates and pebbly reddish brown sand with silt
FA8	Gray to brown muds and/or silt, including mottled textures and rootlets
FA9	Green-gray, often pebbly sandstone/silt
FA10	Interbedded mud/silt and decimeter-thick sand beds
FA11	Interbedded mud/silt and centimeter-thick sand beds
FA12	Light gray to buff homogeneous to weakly stratified bioturbated mud
FA13	Contorted bedding and mud-supported sand and conglomerates
FA14	Greenish gray pebbly silt and clast-supported fining-upward conglomerates
FA15	Greenish to buff bioclastic laminated silt to bedded fine sand, including bioturbation, ostracods, and rootlets
FA16	Greenish to buff bedded and bioturbated bioclastic sand to mud
FA17	Greenish to buff laminated to faintly bedded/homogeneous fossiliferous mud

Figure F1. Corinth rift with primary rift-related faults (both active and currently inactive), multibeam bathymetry of the gulf, and Expedition 381 drill sites. Offshore fault traces are derived from Nixon et al. (2016), building on Bell et al. (2009) and Taylor et al. (2011). Onshore fault traces are derived from Ford et al. (2007, 2013) and Skourtsos and Kranis (2009). Inset: tectonic setting of Corinth rift in Aegean region, Eastern Mediterranean Sea. Bathymetry data provided by the Hellenic Centre for Marine Research and collected for R/V *Aegaeo* cruises (Sakellariou et al., 2007).

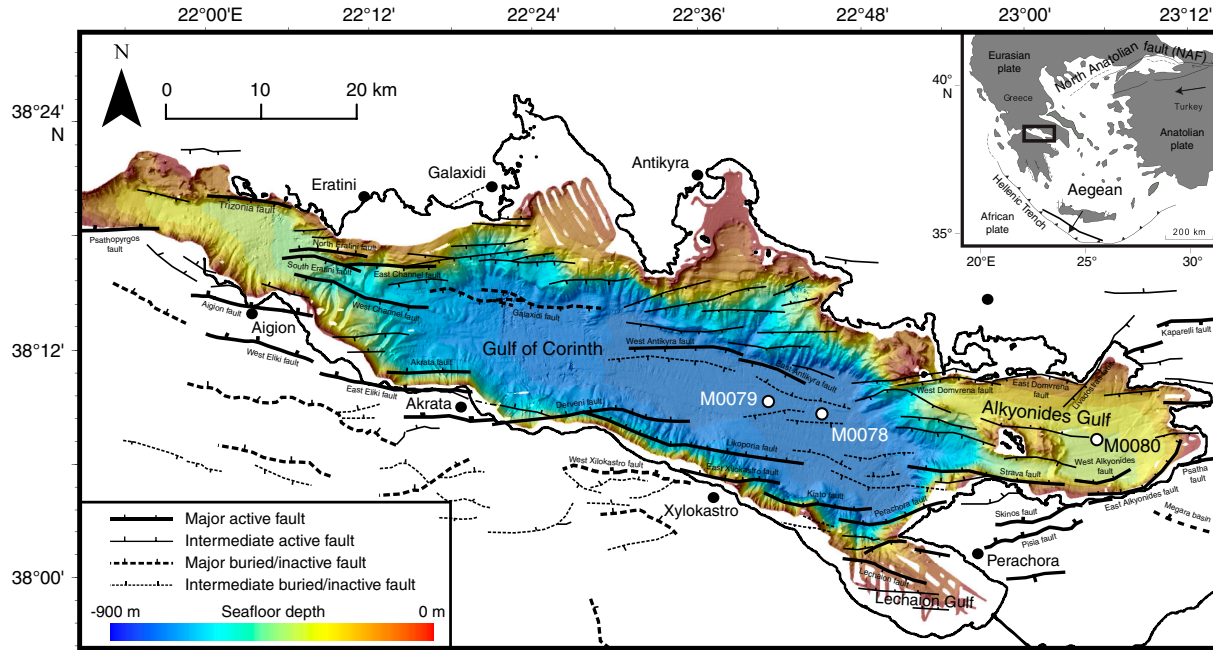


Figure F2. Three proposed rift phases of the Corinth rift system and currently resolved distribution of rift basins for each phase (after Higgs, 1988) with regional fault map overlain (Nixon et al., 2016) (see Figure F1 for map details).

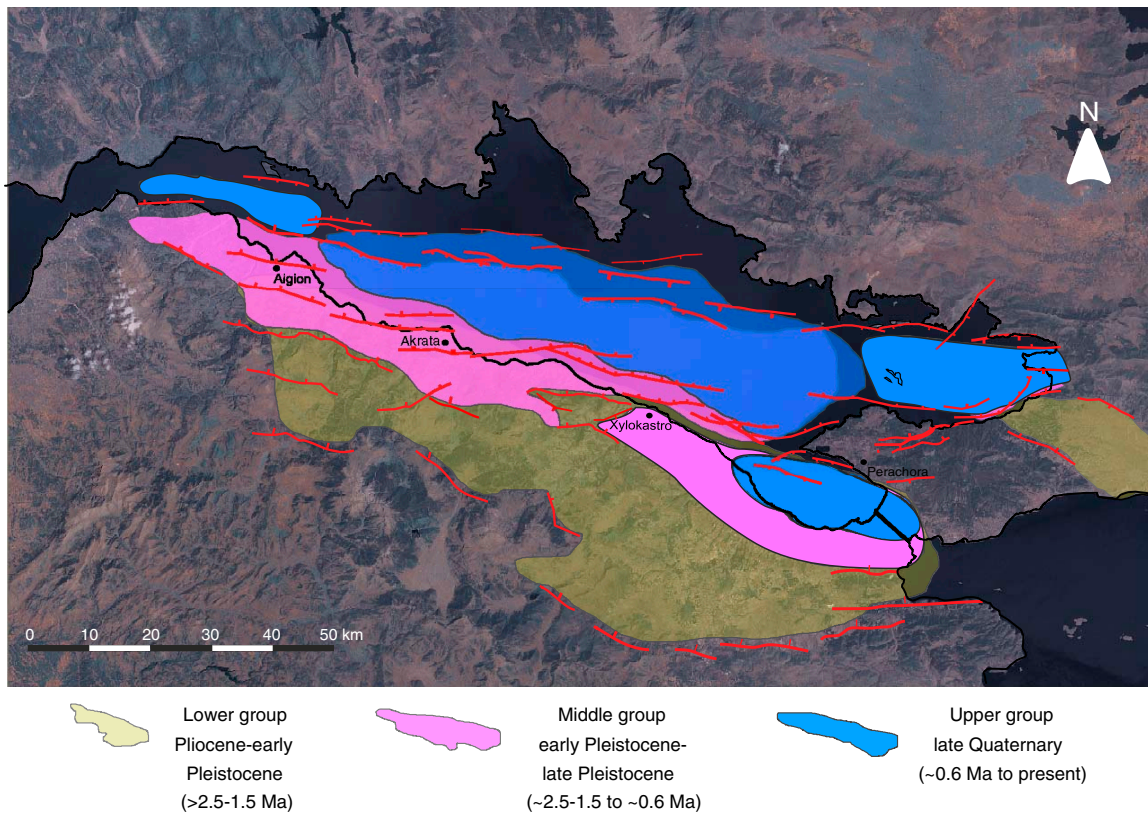


Figure F3. Isochore maps for synrift sequence offshore showing the two primary stratigraphic units separated by regional unit boundary (Bell et al., 2009; Taylor et al., 2011; Nixon et al., 2016). A. Seismic Unit 1 (preregional seismic unit boundary or unconformity, likely equivalent to onshore Middle Group, and estimated age of ~0.6 Ma or older). B. Seismic Unit 2 (postregional seismic unit boundary or unconformity, likely equivalent to onshore Upper Group, and estimated age of ~0.6 Ma or younger). Faults represent those dominantly active during the time period shown. Ages given are predrilling and based on seismic stratigraphic interpretations only. NEF = North Eratini fault, SEF = South Eratini fault, WCF = West Channel fault, ECF = East Channel fault, AIG = Aigion fault, GAL = Galaxidi fault, WEF = West Eliki fault, EEF = East Eliki fault, AKR = Akrata fault, DER = Derveni fault, WAN = West Antikyra fault, LIK = Likoporia fault, WXF = West Xylokastro fault, EXF = East Xylokastro fault, EAN = East Antikyra fault, KIA = Kiato fault, VRA = Vroma fault, PER = Perachora fault, LEX = Lechaion fault, HER = Heraion fault, WDF = West Domvrena fault, STR = Strava fault, PF = Pisias fault, EDF = East Domvrena fault, SKI = Skinios fault, LIV = Livadostras fault, WAF = West Alkyonides fault, EAF = East Alkyonides fault, KAP = Kaparelli fault, PSF = Psatha fault.

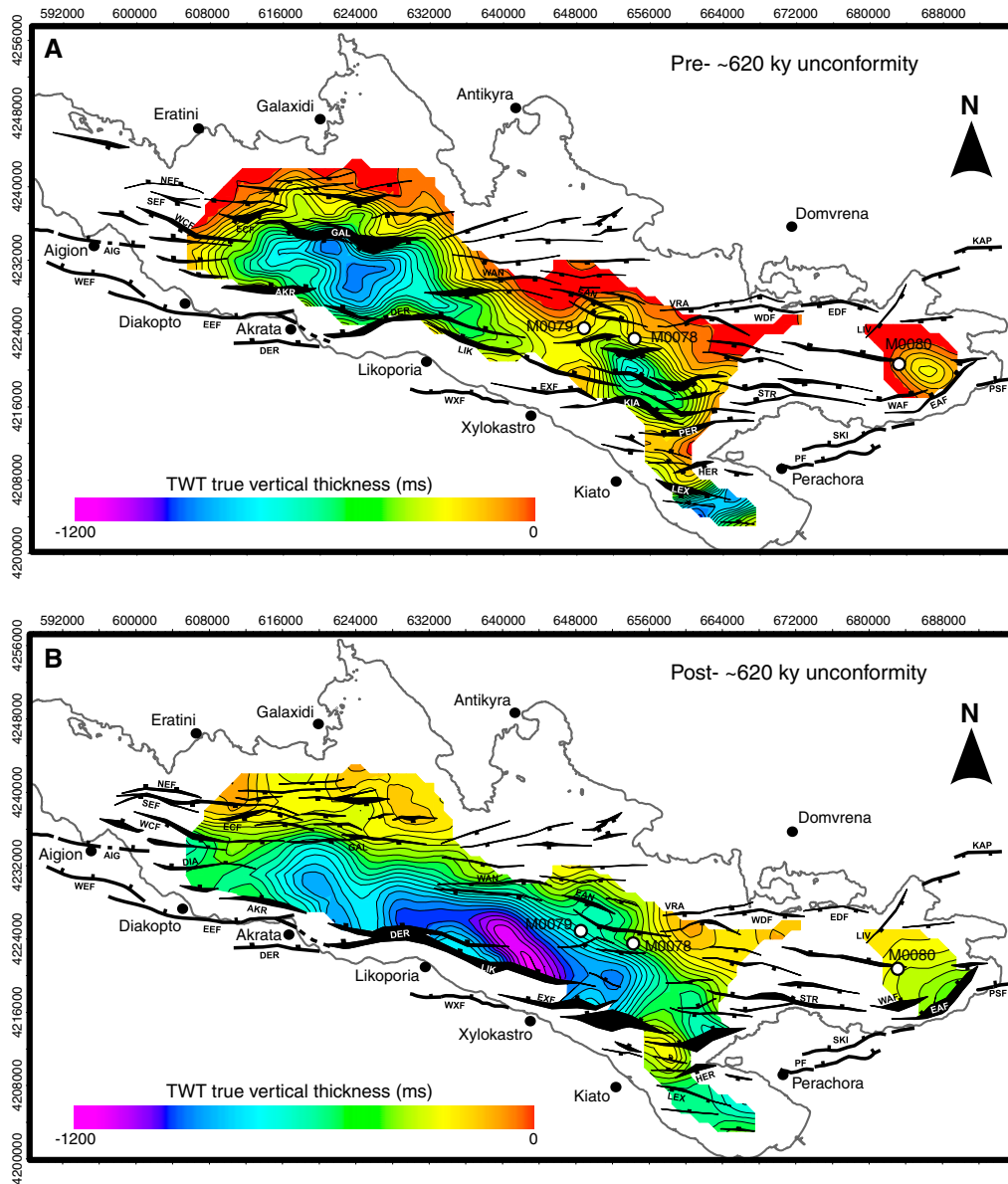


Figure F4. Composite seismic line comprising R/V *Maurice Ewing* Lines 18, 42, and 22 (Taylor et al., 2011), and interpretations of basement (black dotted line) and boundary between seismic Unit 1 (below) and seismic Unit 2 (above) (blue dotted line) from Nixon et al. (2016). Inset: seismic line and drill site locations. CDP = common depth point.

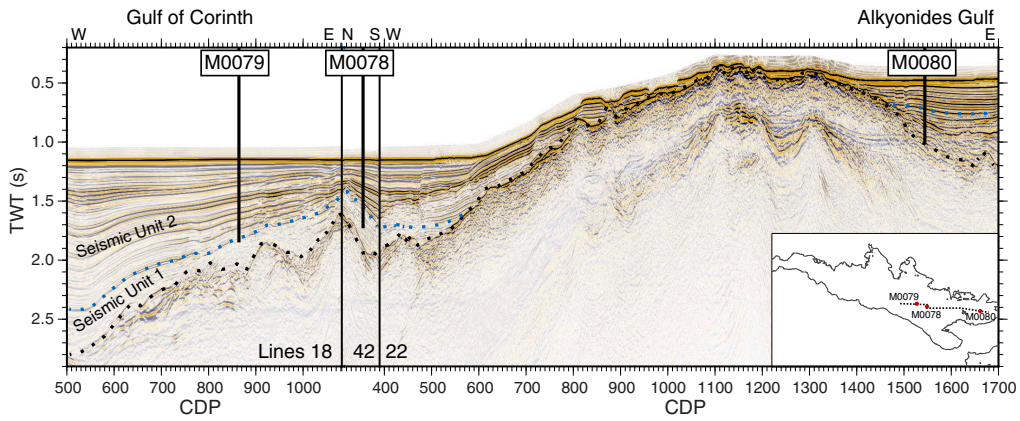


Figure F5. Site M0078 shown with R/V *Maurice Ewing* Line 42 (Taylor et al., 2011) and interpretations from Nixon et al. (2016) (colored dotted lines and text). Inset: seismic line and drill site locations.

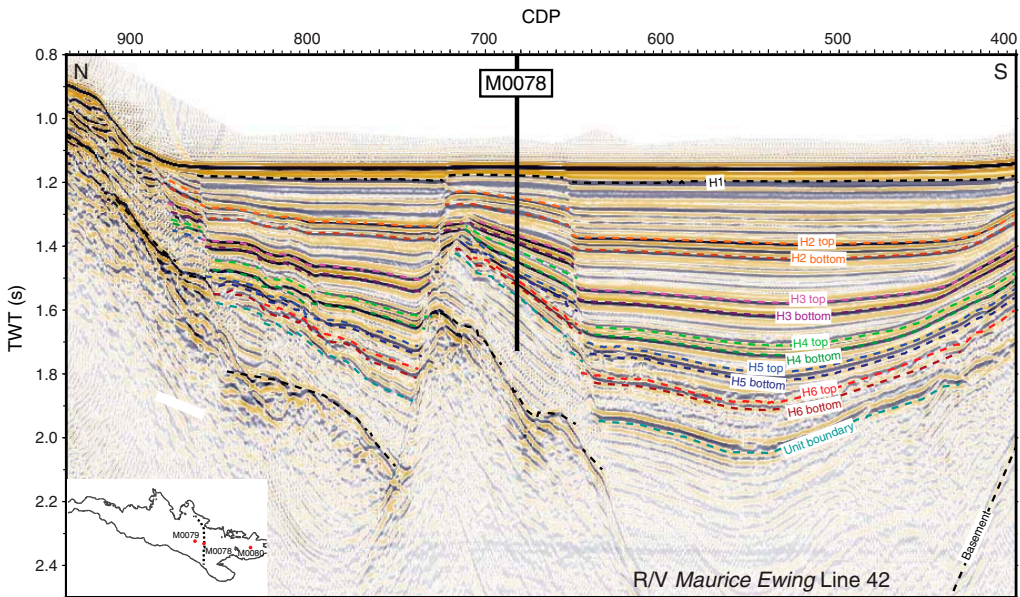


Figure F6. Site M0079 shown with R/V *Maurice Ewing* Line 41 (Taylor et al., 2011) and interpretations from Nixon et al. (2016) (colored dotted lines and text). Inset: seismic line and drill site locations.

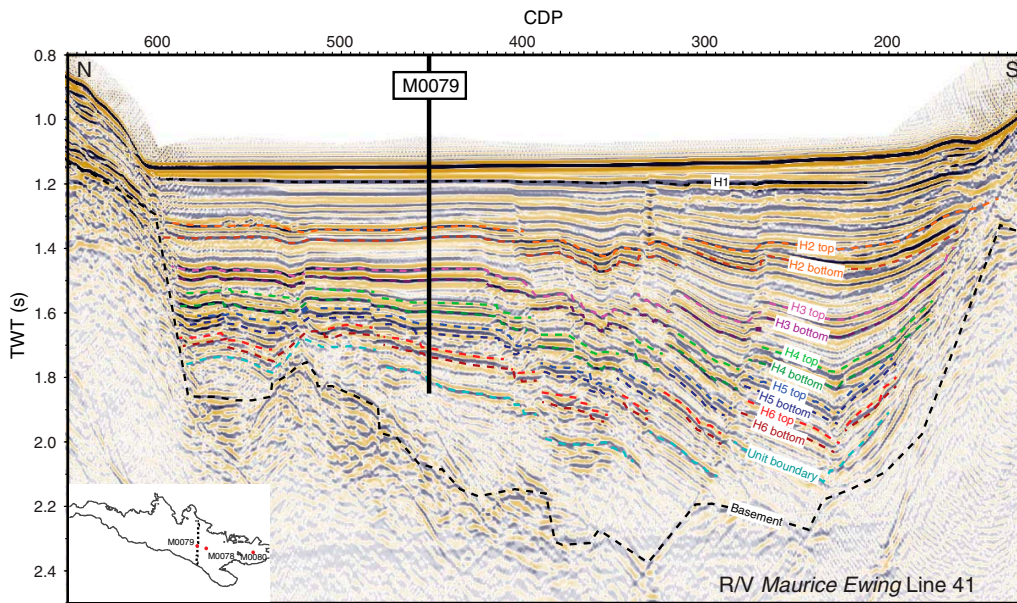


Figure F7. Site M0080 shown with R/V *Maurice Ewing* Line 22 (Taylor et al., 2011) and interpretations from Nixon et al. (2016) (colored dotted lines and text). Inset: seismic line and drill site locations.

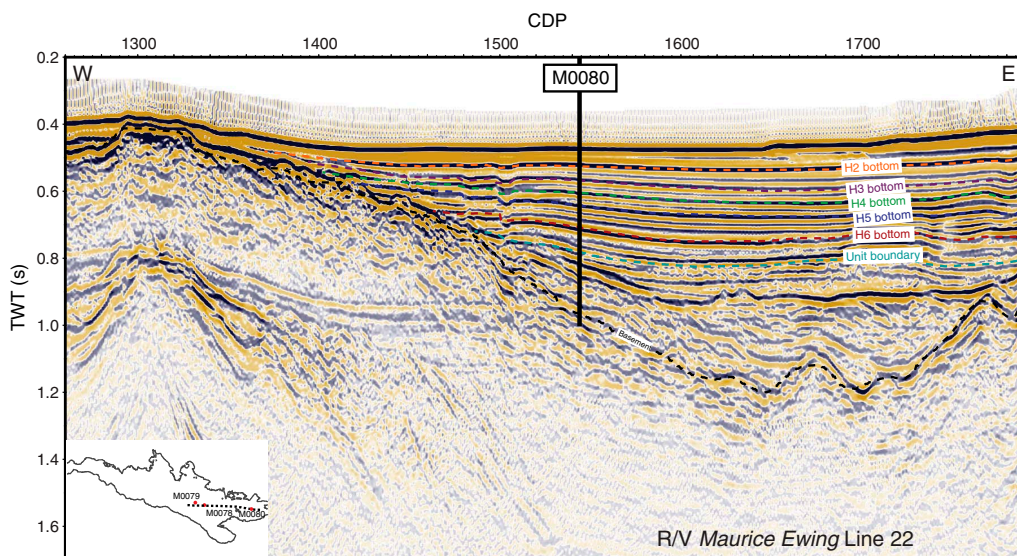


Figure F8. Site M0078 summary. Estimated age. Seismic reflection data crossing site location from Taylor et al. (2011). Lithostratigraphic units and Unit 1 sub-units with paleoenvironment: blue = marine, green = isolated/semi-isolated, gray = undetermined. Lithology/facies associations (FAs) are from lithostratigraphic interpretations (facies associations are grouped for simplicity and coarser sediment layers are highlighted by longer bars); see Table T3 for description of facies associations. MSCL magnetic susceptibility (MS), natural gamma ray (NGR), and density data are from whole cores. MAD bulk density data are from discrete core samples. cps = counts per second.

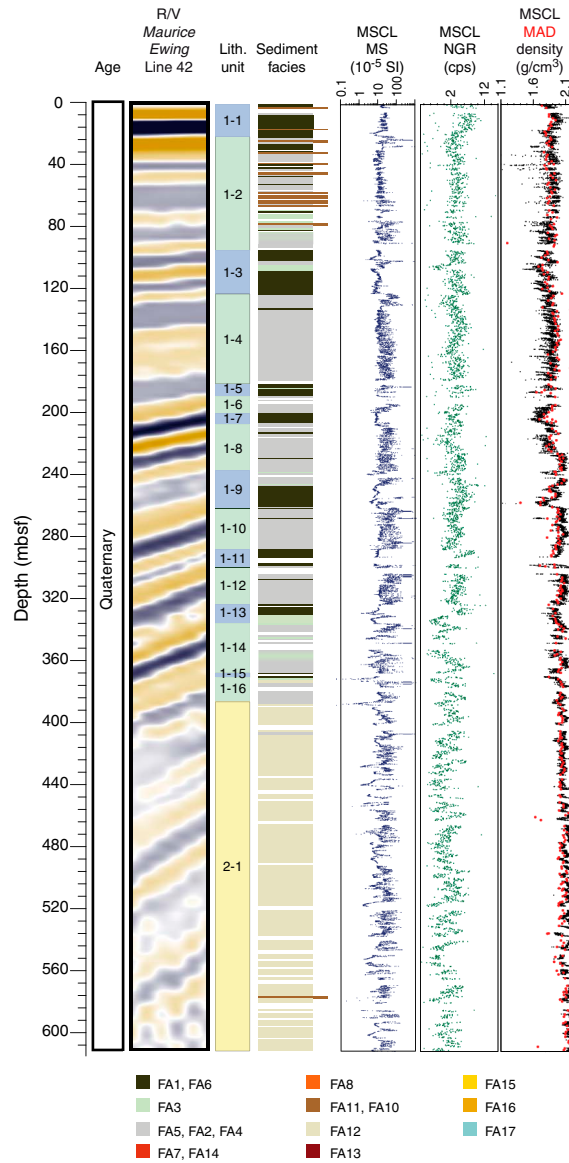


Figure F9. Site M0079 summary. Estimated age. Seismic reflection data crossing site location from Taylor et al. (2011). Lithostratigraphic units and Unit 1 sub-units with paleoenvironment: blue = marine, green = isolated/semi-isolated, gray = undetermined, pink = slumped interval. Lithology/facies associations (FAs) are from lithostratigraphic interpretations (facies associations are grouped for simplicity and coarser sediment layers are highlighted by longer bars); see Table T3 for description of facies associations. MSCL MS, NGR, and density data are from whole cores. MAD bulk density data are from discrete core samples.

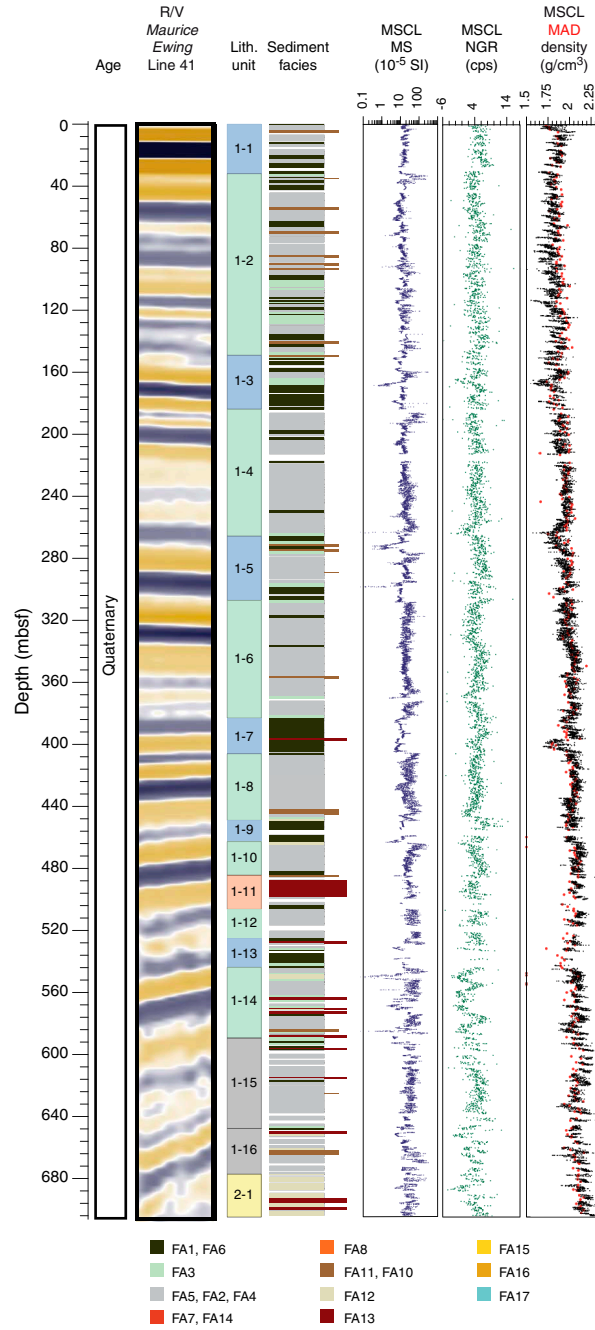


Figure F10. Site M0080 summary. Estimated age. Seismic reflection data crossing site location from Taylor et al. (2011). Lithostratigraphic units and Unit 1 subunits with paleoenvironment: blue = marine, green = isolated/semi-isolated, gray = undetermined. Lithology/facies associations (FAs) are from lithostratigraphic interpretations (facies associations are grouped for simplicity and coarser sediment layers are highlighted by longer bars); see Table T3 for description of facies associations. MSCL MS, NGR, and density data are from whole cores. MAD bulk density data are from discrete core samples.

